Self-similar solution of a supercritical two-phase laminar mixing layer

Jordi Poblador-Ibanez[1],[*], Branson W. Davis[2], William A. Sirignano[3]

University of California, Irvine, CA 92697-3975, United States

ARTICLE INFO

ABSTRACT

Previous works for a liquid suddenly contacting a gas at a supercritical pressure show the coexistence of both phases and the generation of diffusion layers on both sides of the liquid-gas interface due to local thermodynamic phase equilibrium. A related numerical study of a laminar mixing layer between the liquid and gas streams in the near field of the splitter plate suggests that mass, momentum and thermal diffusion layers evolve in a self-similar manner at very high pressures. In this paper, the high-pressure, two-phase, laminar mixing-layer equations are recast in terms of a similarity variable. A liquid hydrocarbon and gaseous oxygen are considered. Freestream conditions and proper matching conditions at the liquid-gas interface are applied. To solve the system of equations, a real-fluid thermodynamic model based on the Soave-Redlich-Kwong equation of state is selected. A comparison with results obtained by directly solving the laminar mixing-layer equations shows the validity of the similarity approach applied to non-ideal two-phase flows. Even when the gas is hotter than the liquid, net condensation can occur at high pressures while heat conducts into the liquid. Finally, a generalized correlation is proposed to represent the evolution of the mixing layer thickness for different problem configurations.

© 2020 Elsevier Ltd. All rights reserved.

1. Introduction

Combustion chambers used in many engineering applications (e.g., power units, gas turbines or liquid-propellant rockets) are designed to operate at elevated pressures. That is, a thermodynamic regime is sought where less dissociation of the reaction products occurs and a better combustion efficiency and specific energy conversion are obtained. In many situations, the chamber pressure is well above the critical pressure of the liquid fuel that is being injected. Well-known fuels are based on hydrocarbon mixtures (e.g., diesel fuel, Jet A, RP-1) with critical pressures around 20 bar, while operating pressures may range from 25 to 40 bar in diesel engines or gas turbines and 70 to 200 bar in rocket engines.

The performance of the combustion reaction also depends on how fast the liquid fuel vaporizes and mixes with the surrounding oxidizer. Therefore, understanding the physical phenomena involved in this process is necessary for a proper design of the injectors' shape and distribution, combustion chamber size, etc. At

subcritical pressures, a clear distinction exists between liquid and gas phases, which allows for extensive experimental studies. However, for near-critical or supercritical pressures, experimental studies show that a thermodynamic transition occurs where the liquid and gas present similar fluid properties near the liquid-gas interface, which is suddenly immersed in a variable-density layer and is rapidly affected by turbulence (Mayer and Tamura, 1996; Mayer et al., 1998; 2000; Chehroudi et al., 2002b; 2002a; Oschwald et al., 2006; Segal and Polikhov, 2008; Chehroudi, 2012; Falgout et al., 2016).

Past works have described this behavior as a very fast transition of the liquid phase to a supercritical state, assuming that a two-phase behavior cannot be sustained under these thermodynamic conditions as suggested by experimental results where a gas-like turbulent structure is observed (Spalding, 1959; Rosner, 1967). But evidence of a two-phase behavior at supercritical pressures in multicomponent fluids exists based on a requirement of thermodynamic phase equilibrium at the liquid-gas interface (Hsieh et al., 1991; Delplanque and Sirignano, 1993; Yang and Shuen, 1994; Sirignano et al., 1997; Jordà-Juanós and Sirignano, 2015; Poblador-Ibanez and Sirignano, 2018). At supercritical pressures, phase equilibrium enhances the dissolution of the gas into the liquid phase, thus generating diffusion layers on both sides of the liquid-gas interface where strong variations of fluid properties occur. Mixture critical properties near the interface differ from pure fluid critical properties and, in general, the new critical pressure is higher

* Corresponding author.
  E-mail address: poblador@uci.edu (J. Poblador-Ibanez).
[1] Graduate Student Researcher, Department of Mechanical and Aerospace Engineering.
[2] Undergraduate Student Researcher, Department of Mechanical and Aerospace Engineering.
[3] Professor, Department of Mechanical and Aerospace Engineering.

than the chamber pressure. However, this does not seem to be a requirement to sustain two phases under very high pressures as discussed in Poblador-Ibanez and Sirignano (2018). Some authors suggest caution at interface temperatures near the critical temperature of the mixture at very high pressures, where the liquid-gas interface enters a continuum region of a few nanometers thickness (Dahms and Oefelein, 2013; 2015a). In this scenario, the interface departs from local thermodynamic equilibrium and a diffuse transition between both phases occurs (Dahms and Oefelein, 2015b). Accordingly, a two-phase behavior cannot exist. Nevertheless, at lower interface temperatures diffusion around the interface occurs rapidly enough to reach diffusion layer thicknesses of the order of micrometers while phase equilibrium is well established (Poblador-Ibanez and Sirignano, 2018). Thus, the interface may still be treated as a discontinuity under phase equilibrium with a clear jump in fluid properties across it, similar to how a compressive shock wave is considered as a discontinuity in compressible fluids. In that case, the non-equilibrium layer thickness for the shock is an order of magnitude or more greater than the layer thickness for phase non-equilibrium.

There are further reasons that support the fact that liquid injection at supercritical pressures is still a two-phase problem. Surface tension forces are reduced at very high pressures due to both phases presenting similar densities at the interface. Therefore, the aerodynamic effects on the liquid breakup process are enhanced (Yang, 2000). Moreover, mixing causes the liquid viscosity to drop to gas-like values near the interface, reducing viscous damping of surface instabilities (Poblador-Ibanez and Sirignano, 2019). Altogether, fast growing instabilities associated with smaller wavelengths develop at the interface, which may cause a very fast atomization of the liquid jet with a cloud of very small droplets around it. This reasoning is further supported by numerical results of incompressible liquid round jets and planar sheets injected into a gas. For similar liquid and gas densities with reduced surface tension, a fast breakup process is induced with early small droplet formation and enhanced radial development of the two-phase mixture (Jarrahbashi and Sirignano, 2014; Jarrahbashi et al., 2016; Zandian et al., 2017; 2018; 2019). Traditional experimental techniques have difficulties with visual penetration of dense sprays due to the scattering caused by the large amount of small droplets and the intrinsic difficulties of variable-density fluids. Thus, it becomes difficult to distinguish between liquid and gas phases. Some new techniques have been able to penetrate dense sprays and show clear liquid structures (i.e., ligaments, lobes, bigger droplets) emerging from the liquid core, although they have not been tested yet in supercritical environments (Minniti et al., 2018, 2019).

The present work does not address the hydrodynamic instabilities that occur farther downstream as part of the atomization process. It focuses on the initial laminar mixing between the injected liquid and the gas before substantial growth of surface instabilities or transition to turbulence. Understanding how the mixing between both streams evolves is crucial to understand the beginning of high-pressure atomization and can also help create models to use as initial conditions for more complex numerical studies.

Davis et al. (2021) present a two-dimensional numerical study involving the non-ideal two-phase laminar mixing layer equations and provide guidelines on the validity of these relations. Results are presented for a binary mixture where a liquid stream and a gas stream come together at the end of a splitter plate at various ambient pressures, ranging from subcritical to supercritical for the pure liquid. The liquid stream is initially composed by pure n-decane and the gas stream is pure oxygen. The mixing layer thickness grows to a few micrometers in the liquid phase and to tens of micrometers in the gas phase with downstream distance from the end of the splitter plate. At the same time, the interface reaches a near-steady solution sufficiently far away from the splitter plate.

Most importantly, each individual configuration (i.e., each set of boundary conditions) shows signs of a self-similar behavior of the mixing layer evolution, even when the defined mixing layer equations involve non-ideal terms and are coupled to a non-ideal thermodynamic model involving a real-gas equation of state, thermodynamic fundamental principles and various high-pressure correlations. A self-similar behavior in this high-pressure environment is also suggested in Poblador-Ibanez and Sirignano (2018), although in that work a non-ideal unsteady one-dimensional model is implemented.

Reducing the system of partial differential equations (i.e., mixing layer equations) to a system of ordinary differential equations in terms of a similarity variable is of special interest, not only because a simplified mathematical model describing the same phenomena is obtained, but also because of the fundamental analysis implied in the transformation. Similarity solutions have always been sought in classical fluid mechanics (e.g., the Blasius solution for the flow over a flat plate or the Falker-Skan wedge flows), usually limited to incompressible flows. Some transformations are also available for compressible flows or flows with variable fluid properties, although simplifications are made to obtain a generic self-similar model (e.g., use of ideal-gas model). In general, these approaches are well documented in textbooks (White and Corfield, 2006; Williams, 2018). When analyzing compressible or variable-density laminar shear layers, the focus is usually limited to single-phase configurations under ideal-gas assumptions with momentum and thermal mixing. However, some works also include species mixing in their analysis (Kennedy and Gatski, 1994).

In views of the discussed numerical results (Poblador-Ibanez and Sirignano, 2018; Davis et al., 2021), the non-ideal two-phase laminar mixing layer equations presented in Section 2 are recast in terms of a similarity variable in Section 3, thus forming a system of ordinary differential equations. Boundary conditions and liquid-gas interface matching relations are provided in Section 4, which allow for mass, momentum and energy transfer across the interface to occur. Section 5 presents the numerical approach followed to solve the self-similar system of equations. Then, the self-similar model is coupled to a non-ideal thermodynamic model to close the system of equations. The self-similar solution is compared in Sections 6.1 and 6.2 against the results from Davis et al. (2021) with different problem configurations to assess the validity of the self-similar model. Finally, a proper non-dimensional scaling is presented in Section 6.3, which provides a semi-collapse of the self-similar solutions for different sets of boundary conditions. This allows the development of a correlation based on freestream and interface conditions which is able to estimate mixing layer thicknesses with sufficient accuracy.

2. Non-ideal two-phase laminar mixing layer equations

The behavior of two parallel streams coming together at the edge of a splitter plate can be modeled under the boundary-layer approximation after a transitional region (White and Corfield, 2006). For a sufficiently large Reynolds number, the flow begins to develop with the transverse velocity being much smaller than the streamwise velocity, $v \ll u$, and variations in the x-direction become negligible compared to variations in y (i.e., $\partial()/\partial x \ll \partial()/\partial y$). The transverse pressure gradient, $\partial p/\partial y$, is also negligible. Therefore, the transverse velocity solution is directly obtained from the continuity equation and not from the transverse momentum equation (He and Ghoniem, 2017; Poblador-Ibanez and Sirignano, 2018). For free-shear, low-Mach number flows at high pressures without confining walls, pressure can be assumed constant ($Dp/Dt = \partial p/\partial x = \partial p/\partial y = 0$). Furthermore, viscous dissipation and kinetic energy can be safely neglected in the energy equation.

Both fluid streams are initially pure components (e.g., a pure liquid hydrocarbon and a pure gas, such as oxygen). The governing equations are cast in non-conservative form and in terms of the mass fraction of one mixture component, Y_1, where $Y_1 + Y_2 = 1$. Under these conditions, the steady-state governing equations describing the two-phase laminar mixing layer development of two non-ideal fluids (i.e., a liquid stream and a gas stream) are the continuity equation, Eq. (1), streamwise momentum equation, Eq. (2), species continuity equation, Eq. (3), and energy equation, Eq. (4). For simplicity, a Fickian form is used to represent mass diffusion in Eqs. (3) and (4) since a binary mixture is considered. The system of equations is given as

$$\frac{\partial}{\partial x}(\rho u) + \frac{\partial}{\partial y}(\rho v) = 0 \tag{1}$$

$$\rho u \frac{\partial u}{\partial x} + \rho v \frac{\partial u}{\partial y} = \frac{\partial}{\partial y}\left(\mu \frac{\partial u}{\partial y}\right) \tag{2}$$

$$\rho u \frac{\partial Y_1}{\partial x} + \rho v \frac{\partial Y_1}{\partial y} = \frac{\partial}{\partial y}\left(\rho D \frac{\partial Y_1}{\partial y}\right) \tag{3}$$

$$\rho u \frac{\partial h}{\partial x} + \rho v \frac{\partial h}{\partial y} = \frac{\partial}{\partial y}\left(\frac{\lambda}{c_p}\frac{\partial h}{\partial y}\right) + \frac{\partial}{\partial y}\left[\left(\rho D - \frac{\lambda}{c_p}\right)(h_1 - h_2)\frac{\partial Y_1}{\partial y}\right] \tag{4}$$

where ρ, u and v are the mixture density, streamwise velocity and transverse velocity, respectively. h is the mixture specific enthalpy and h_1 and h_2 are the partial specific enthalpies of each species of the binary mixture. Other mixture fluid properties are the mixture dynamic viscosity, μ, the mass diffusion coefficient, D, the thermal conductivity, λ, and the specific heat at constant pressure, c_p. Furthermore, the energy equation is written as an enthalpy transport equation by using the relation $\lambda \nabla T = (\lambda/c_p)\nabla h - \sum_{i=1}^{N}(\lambda/c_p)h_i\nabla Y_i$. Note that since the problem is diffusion-driven, fluid properties will vary as species and energy diffuse.

These steady-state equations are valid as long as the flow is laminar and surface instabilities are negligible. Davis et al. (2021) provide some guidance for oxygen-hydrocarbon mixtures at various ambient pressures. The quasi-parallel laminar region may exist up to a distance from the splitter plate of the order of $\mathcal{O}(10^{-2}$ m). The mean flow velocity is fixed at 10 m/s and the velocity difference between both streams is varied in the range of $\Delta u = 0.3 - 5$ m/s to limit the maximum Reynolds number at $\bar{L} = 0.01$ m to $Re_{\bar{L}} = 10,000$. $Re_{\bar{L}}$ is defined as in Davis et al. (2021)

$$Re_{\bar{L}} = \frac{\rho_G \bar{L} \Delta u}{\mu_G} \tag{5}$$

where the subscript G refers to gas freestream values. Analogously, the subscript L will refer to liquid freestream values.

With this analysis, one of the main goals is to show the existence of a distinct two-phase behavior before hydrodynamic instabilities dominate.

3. Similarity transformation

The system of partial differential equations (PDEs) describing the problem (Eqs. (1)–(4)) can be transformed into a system of ordinary differential equations (ODEs) by using a proper similarity variable, η. However, the transformation requires an intermediate step due to variable density. The mapping follows $(x, y) \rightarrow (\bar{x}, z) \rightarrow \eta$.

The first transformation is defined as

$$\bar{x} = x \quad ; \quad z = \int_0^y \rho \, dy' \tag{6}$$

where y' is a dummy variable for integration purposes and z is a density-weighted transverse coordinate following the so-called Howarth-Dorodnitsyn transformation (Williams, 2018). This type of transformation was independently introduced in 1942 by Dorodnitsyn (1942) and later in 1948 by Howarth (1948). Other authors followed with similar work (Stewartson, 1949; Lees, 1956).

As shown in Fig. 1, the interface between the two phases is placed at $y = 0$. To transform the original system of equations from $(x, y) \rightarrow (\bar{x}, z)$, the following relations between partial derivatives are obtained

$$\frac{\partial}{\partial x}() = \frac{\partial}{\partial \bar{x}}() + \left(\int_0^y \frac{\partial \rho}{\partial x} dy'\right)\frac{\partial}{\partial z}() \tag{7}$$

$$\frac{\partial}{\partial y}() = \rho \frac{\partial}{\partial z}() \tag{8}$$

Defining the transformed transverse velocity, w, as

$$w = \rho v + u \int_0^y \frac{\partial \rho}{\partial x} dy' \tag{9}$$

the velocity components can be related to the stream function for compressible flow, $\Psi(\bar{x}, z)$, as

$$u = \frac{\partial \Psi}{\partial z} \quad ; \quad w = -\frac{\partial \Psi}{\partial \bar{x}} \tag{10}$$

Here, w does not have units of velocity and can be considered as a convenient variable in the solution process.

This arrangement yields a system of PDEs in the $(\bar{x}, z)$ space in terms of the compressible stream function, Eqs. (11)–(14). Note the continuity equation, Eq. (11), is identically satisfied.

$$\frac{\partial^2 \Psi}{\partial \bar{x} \partial z} - \frac{\partial^2 \Psi}{\partial z \partial \bar{x}} = 0 \tag{11}$$

$$\frac{\partial \Psi}{\partial z}\frac{\partial^2 \Psi}{\partial \bar{x} \partial z} - \frac{\partial \Psi}{\partial \bar{x}}\frac{\partial^2 \Psi}{\partial z^2} = \frac{\partial}{\partial z}\left(\rho\mu\frac{\partial^2 \Psi}{\partial z^2}\right) \tag{12}$$

$$\frac{\partial \Psi}{\partial z}\frac{\partial Y_1}{\partial \bar{x}} - \frac{\partial \Psi}{\partial \bar{x}}\frac{\partial Y_1}{\partial z} = \frac{\partial}{\partial z}\left(\rho^2 D\frac{\partial Y_1}{\partial z}\right) \tag{13}$$

$$\frac{\partial \Psi}{\partial z}\frac{\partial h}{\partial \bar{x}} - \frac{\partial \Psi}{\partial \bar{x}}\frac{\partial h}{\partial z} = \frac{\partial}{\partial z}\left(\frac{\rho\lambda}{c_p}\frac{\partial h}{\partial z}\right) + \frac{\partial}{\partial z}\left[\left(\rho^2 D - \frac{\rho\lambda}{c_p}\right)(h_1 - h_2)\frac{\partial Y_1}{\partial z}\right] \tag{14}$$

After this intermediate step, the self-similar transformation is taken by defining the similarity variable, η, as in the Blasius solution for a flat plate (White and Corfield, 2006), but where x is substituted by $\bar{x}$ and y is substituted by z (see Eq. (15)).

$$\eta = \frac{z}{\sqrt{2\bar{x}}} \tag{15}$$

The transformation from $(\bar{x}, z) \rightarrow \eta$ requires the following relations between partial derivatives

$$\frac{\partial}{\partial z}() = \frac{1}{\sqrt{2\bar{x}}}\frac{\partial}{\partial \eta}() \tag{16}$$

$$\frac{\partial}{\partial \bar{x}}() = \frac{\partial}{\partial \bar{\bar{x}}}() - \frac{1}{2}\frac{\eta}{\bar{x}}\frac{\partial}{\partial \eta}() \tag{17}$$

where $\bar{\bar{x}} = \bar{x} = x$.

A self-similar solution exists if $\Psi/\sqrt{\bar{x}}$, Y_1 and h depend only on η. The following expressions are assumed, where

$$\Psi = \sqrt{2\bar{x}}f(\eta) \quad ; \quad Y_1 = Y(\eta) \quad ; \quad h = h(\eta) \tag{18}$$

From Eq. (10), it reads that

$$u = \frac{df}{d\eta} = f'(\eta) \quad ; \quad w = \frac{1}{\sqrt{2\bar{x}}}\left(\eta f'(\eta) - f(\eta)\right) \tag{19}$$
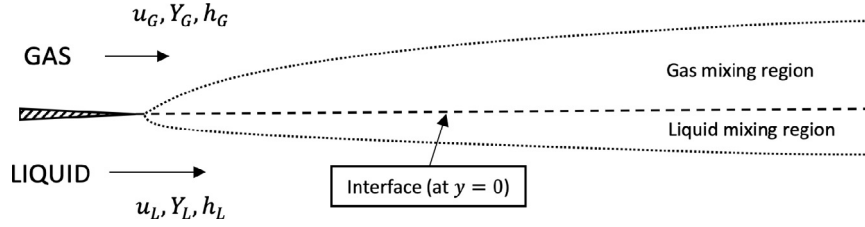
Fig. 1. Sketch of the mixing layer problem between a liquid stream and a gas stream. The liquid-gas interface or dividing streamline is assumed to be fixed at $y = 0$ m as discussed in Davis et al. (2021).

where the $(\ )'$ operator applied to any variable a (i.e., a') means differentiation of a with respect to η or $da/d\eta$. Second and third derivatives follow the same notation. For the sake of simplicity, single dependence on η is implicit in the equations to follow.

Rearranging Eqs. (12)–(14), a system of ODEs can be written as

$$(\rho\mu)f''' + (\rho\mu)'f'' + ff'' = 0 \tag{20}$$

$$(\rho^2 D)Y'' + (\rho^2 D)'Y' + fY' = 0 \tag{21}$$

$$\left(\frac{\rho\lambda}{c_p}\right)h'' + \left(\frac{\rho\lambda}{c_p}\right)'h' + \left(\rho^2 D - \frac{\rho\lambda}{c_p}\right)(h_1 - h_2)Y''$$

$$+ \left[\left(\rho^2 D - \frac{\rho\lambda}{c_p}\right)(h_1 - h_2)\right]'Y' + fh' = 0 \tag{22}$$

3.1. Evaluation of the transverse velocity

The determination of the transverse velocity, v, across the mixing layer from the self-similar solution in variable-density mixing layers has been given little to no attention in previous works and textbooks. Generally, the interest is only focused on solving the velocity profile in the main flow direction, together with the mixing profiles of other variables such as density and temperature. Some works addressing this issue are those of Kennedy and Gatski (1994) and Libby and Liu (1968). However, relations for v are presented without further development. On the other hand, Pruett (1993) offers some insights in the process to develop such relations. Nevertheless, the analysis performed on the boundary layer of an axisymmetric body complicates the final result.

In the present study, a straightforward development of an equation for v based on η and downstream location is presented in a form also shown in Sirignano (2021). The latter work develops a self-similar model for mixing in a variable-density laminar shear layer with imposed counterflow.

Eqs. (8) and (16) provide a differential relation between y and η for a fixed downstream position or constant $\bar{x}$ which can be integrated to relate the transverse location to the similarity variable as

$$dy = \frac{\sqrt{2\bar{x}}}{\rho}d\eta \quad ; \quad y = \sqrt{2\bar{x}}\int_0^\eta \frac{d\eta'}{\rho(\eta')} = \sqrt{2\bar{x}}\tilde{I}(\eta) \tag{23}$$

where η' is a dummy variable for integration purposes and $\tilde{I}(\eta) \equiv \int_0^\eta d\eta'/\rho(\eta')$.

By combining expressions of the transformed transverse velocity, w, in (x, y) and $(\bar{x}, \eta)$ coordinates (Eqs. (9) and (19)), the following relation is obtained

$$w\sqrt{2\bar{x}} = \rho v\sqrt{2\bar{x}} + u\sqrt{2\bar{x}}\frac{\partial z}{\partial x} = \eta f' - f \tag{24}$$

which shows that w (and thus v) are self-similar when multiplied by the square root of $\bar{x}$ or downstream position. In the previous equation, the equality $\int_0^y (\partial\rho/\partial x)dy' = \partial(\int_0^y \rho dy')/\partial x = \partial z/\partial x$ is used.

Substitution of $\partial z/\partial x$ in Eq. (24) is found by differentiating dy/dx, dz/dx and $dz/d\bar{x}$ at constant y using Eq. (7).

$$\frac{dy}{dx} = 0 = \frac{dy}{d\bar{x}} + \frac{1}{\rho}\frac{dz}{dx} = \tilde{I}\frac{d}{d\bar{x}}(\sqrt{2\bar{x}}) + \frac{\sqrt{2\bar{x}}}{\rho}\frac{d\eta}{d\bar{x}} + \frac{1}{\rho}\frac{dz}{dx} \tag{25}$$

$$\frac{dz}{dx} = \frac{dz}{d\bar{x}} + \frac{dz}{dx} \quad \rightarrow \quad \frac{dz}{d\bar{x}} = 0 \tag{26}$$

$$\frac{dz}{d\bar{x}} = 0 = \sqrt{2\bar{x}}\frac{d\eta}{d\bar{x}} + \eta\frac{d}{d\bar{x}}(\sqrt{2\bar{x}}) \tag{27}$$

Combination of Eqs. (25) and (27) yields a relation for dz/dx, Eq. (28). This relation can be substituted back into Eq. (24) to find an equation for the transverse velocity v as a function of self-similar variables and downstream position, Eq. (29).

$$\frac{dz}{dx} = \left(\eta - \tilde{I}\rho\right)\frac{d}{d\bar{x}}(\sqrt{2\bar{x}}) \tag{28}$$

$$\rho v\sqrt{2\bar{x}} = \tilde{I}\rho f' - f \tag{29}$$

3.2. Comments on the thermodynamic model

Another requirement needed to achieve similarity relates to the thermodynamic model used to evaluate fluid properties and transport coefficients. For these variables to depend only on η, the thermodynamic model must ultimately depend on pressure, temperature (i.e., enthalpy) and mixture composition. The self-similar model presented here relies on constant pressure everywhere in the domain, while temperature and mixture composition depend only on η.

The thermodynamic model implemented in this work is based on a volume-corrected Soave-Redlich-Kwong (SRK) cubic equation of state (Lin et al., 2006), which is able to represent non-ideal fluid states. The volumetric correction is needed to obtain accurate density predictions of high-density fluids (i.e., liquids) because the original SRK equation of state (Soave, 1972) presents liquid density errors of up to 20% when compared to experimental values (Yang, 2000; Prausnitz and Tavares, 2004). The modified SRK equation of state is expressed in terms of the compressibility factor, Z, as

$$Z^3 + (3C - 1)Z^2 + \left[C(3C - 2) + A - B - B^2\right]Z$$

$$+ C(C^2 - C + A - B - B^2) - AB = 0 \tag{30}$$

with

$$Z = \frac{p}{\rho RT} \quad ; \quad A = \frac{a(T)p}{R_u^2 T^2} \quad ; \quad B = \frac{bp}{R_u T} \quad ; \quad C = \frac{c(T)p}{R_u T} \tag{31}$$

where $a(T)$ is a temperature-dependent cohesive energy parameter, b represents a volumetric parameter related to the space occupied by the molecules and $c(T)$ is a temperature-dependent volume correction. R and R_u are the specific gas constant and the universal gas constant, respectively. The solution of this cubic equation provides the density of the fluid mixture, ρ.

The volume-corrected SRK equation of state is used, together with high-pressure correlations, to evaluate fluid properties and

transport coefficients (e.g., viscosity) (Poling et al., 2001; Chung et al., 1988; Leahy-Dios and Firoozabadi, 2007). Details on the development and implementation of this thermodynamic model can be found in Davis et al. (2021).

4. Boundary conditions and interface matching relations

The governing equations representing the non-ideal two-phase laminar mixing layer have been reduced to a system of ODEs, Eqs. (20)–(22), which depends only on the similarity variable, η. To solve this system of equations, proper boundary conditions must be imposed. These can be divided into freestream conditions for each individual fluid and interface matching relations between both fluid streams.

The self-similar transformation is defined such that the liquid-gas interface, which is denoted by Γ, does not move ($V_\Gamma = 0$) and is located at $y = z = \eta = 0$. The justification for this approximation has been shown by Davis et al. (2021). Positive values of η define the gas stream, while negative values of η represent the liquid stream. Following this definition, freestream boundary conditions for f, Y and h become

$$f'(+\infty) = u_G \quad ; \quad Y(+\infty) = Y_G \quad ; \quad h(+\infty) = h_G \qquad (32)$$

and

$$f'(-\infty) = u_L \quad ; \quad Y(-\infty) = Y_L \quad ; \quad h(-\infty) = h_L \qquad (33)$$

At $\pm\infty$, both streams are pure components. Thus, if Y_1 is chosen to represent the pure gas species, $Y_G = 1$ and $Y_L = 0$ in Eqs. (32) and (33).

The streamwise velocity component and the tangential stress are continuous across the interface. These conditions are expressed in the original space (x, y) as

$$u_g = u_l = U_\Gamma \qquad (34)$$

$$\mu_g \left(\frac{\partial u}{\partial y} \right)_g = \mu_l \left(\frac{\partial u}{\partial y} \right)_l \qquad (35)$$

which converts in the η space to

$$f'_g(0) = f'_l(0) = U_\Gamma \qquad (36)$$

$$\frac{f''_l(0)}{f''_g(0)} = \frac{(\rho\mu)_g}{(\rho\mu)_l} \qquad (37)$$

Therefore, f' is continuous across the interface while a jump in the second derivative, f'', exists for $(\rho\mu)_g \neq (\rho\mu)_l$. Another condition for f is obtained from the mass balance across the interface. Since the interface location is assumed to remain fixed, the net mass flux, $\dot{\omega}$, across the interface reads

$$\dot{\omega} = (\rho v)_g = (\rho v)_l \qquad (38)$$

Eq. (38) is expressed in terms of $f(\eta)$ as

$$\dot{\omega} = -\frac{1}{\sqrt{2\bar{x}}} f_g(0) = -\frac{1}{\sqrt{2\bar{x}}} f_l(0) \qquad (39)$$

since $\tilde{I} = 0$ at the interface. This equation shows that f is also continuous across the interface (i.e., $f_g(0) = f_l(0) = f(0)$). From this relation, the transformed velocity evaluated at the interface corresponds to the mass flux across it, or $w(0) = \dot{\omega} = -f(0)/\sqrt{2\bar{x}}$.

Finally, expressions for the species mass balance and energy balance at the interface are needed. Eqs. (40) and (41) show these relations in the (x, y) space, respectively.

$$\dot{\omega}(Y_{1,g} - Y_{1,l}) = \left(\rho D \frac{\partial Y_1}{\partial y} \right)_g - \left(\rho D \frac{\partial Y_1}{\partial y} \right)_l \qquad (40)$$

$$\dot{\omega}(h_g - h_l) = \left(\frac{\lambda}{c_p} \frac{\partial h}{\partial y} \right)_g - \left(\frac{\lambda}{c_p} \frac{\partial h}{\partial y} \right)_l + \left[\left(\rho D - \frac{\lambda}{c_p} \right)(h_1 - h_2) \frac{\partial Y_1}{\partial y} \right]_g$$
$$- \left[\left(\rho D - \frac{\lambda}{c_p} \right)(h_1 - h_2) \frac{\partial Y_1}{\partial y} \right]_l \qquad (41)$$

Eqs. (40) and (41) are expressed in terms of $f(\eta)$, $Y(\eta)$ and $h(\eta)$ as

$$-f(0)\left(Y_g(0) - Y_l(0)\right) = \left(\rho^2 DY'(0)\right)_g - \left(\rho^2 DY'(0)\right)_l \qquad (42)$$

$$-f(0)\left(h_g(0) - h_l(0)\right) = \left(\frac{\rho\lambda}{c_p} h'(0) \right)_g - \left(\frac{\rho\lambda}{c_p} h'(0) \right)_l$$
$$+ \left[\left(\rho^2 D - \frac{\rho\lambda}{c_p} \right)(h_1 - h_2)Y'(0) \right]_g$$
$$- \left[\left(\rho^2 D - \frac{\rho\lambda}{c_p} \right)(h_1 - h_2)Y'(0) \right]_l \qquad (43)$$

Local thermodynamic phase equilibrium is used to evaluate the interface solution of the system of ODEs. That is, an equality in chemical potential for each species on either side of the interface is imposed. This condition is expressed through an equality in fugacity for each species (Soave, 1972; Poling et al., 2001), ϕ_i, as

$$\phi_{li}(T_l, p_l, X_{li}) = \phi_{gi}(T_g, p_g, X_{gi}) \qquad (44)$$

which is a function of mixture temperature, pressure and composition. Under constant pressure across the interface, phase equilibrium can be expressed using the fugacity coefficient, $\Phi_i \equiv \phi_i/pX_i$, as

$$X_{li}\Phi_{li} = X_{gi}\Phi_{gi} \qquad (45)$$

where X_i represents the mole fraction of species i.

Note that liquid and gas compositions are only the same at the mixture critical point. Therefore, phase equilibrium shows that Y and h are discontinuous across the interface, as well as other fluid properties (e.g., density).

Since the thickness of the interface is of the order of $\mathcal{O}(10^{-9}$ m) (Dahms and Oefelein, 2013; 2015a) and diffusion layers in non-ideal high-pressure conditions quickly reach thicknesses of the order of $\mathcal{O}(10^{-6}$ m) (Poblador-Ibanez and Sirignano, 2018; Davis et al., 2021), the interface thickness is neglected and temperature is assumed to be continuous (i.e., $T_g(0) = T_l(0) = T_\Gamma$). This is a plausible assumption as long as the interface temperature is well below the mixture critical temperature (Dahms and Oefelein, 2013; 2015b). For the type of mixture analyzed in the present work, the problem configuration (i.e., ambient pressure and temperatures of each phase) result in an interface equilibrium state far away from the mixture critical point as reported in Fig. 5 of Poblador-Ibanez and Sirignano (2018). Moreover, the quick relaxation of the interface solution either in time (Poblador-Ibanez and Sirignano, 2018) or in space (Davis et al., 2021) supports the local thermodynamic equilibrium assumption. The difference between the two mass fluxes crossing the interface in each direction can be considered to be small compared to either flux as shown in Poblador-Ibanez and Sirignano (2018), which also justifies the use of local phase equilibrium.

5. Solution method

The system of ODEs, Eqs. (20)–(22), must be solved numerically. To avoid solving a third-order differential equation, Eq. (20) is split into two equations: a first-order differential equation to solve for f and a second-order differential equation to solve for f'. Therefore, Eq. (20) is rewritten as

$$(\rho\mu)g_1'' + (\rho\mu)'g_1' + g_2 g_1' = 0 \tag{46}$$

$$g_2' = g_1 \tag{47}$$

where the new variables are $g_1 = f'$ and $g_2 = f$.

Eqs. (21), (22), (46) and (47) are discretized using a second-order finite difference scheme and solved using a tri-diagonal matrix solver. The asymptotic behaviors at $+\infty$ and $-\infty$ are well represented with a numerical range for the similarity variable given by $-0.5 \leq \eta \leq 0.5$. Since the system of equations is highly coupled, some iterations are needed before reaching a converged solution. A mesh size of $\Delta\eta = 1.5625 \times 10^{-4}$ kg/(m$^{5/2}$) provides a grid-independent solution.

The interface solution is also updated at every iteration. The streamwise momentum matching conditions, Eqs. (36) and (37), are combined numerically to solve for U_Γ or $f'(0)$. On the other hand, Eqs. (42), (43) and (45) form a closed system that can be solved at every iteration in terms of the interface temperature. The solution of this system of equations provides the interface values for $f(0)$, $Y_g(0)$, $Y_l(0)$, $h_g(0)$ and $h_l(0)$. More information on this interface algorithm is provided in Poblador-Ibanez and Sirignano (2018).

6. Results

The system of ODEs has been solved for the analyzed cases from Davis et al. (2021), where numerical results for a non-ideal two-phase laminar mixing layer using the system of partial differential equations, Eqs. (1)–(4), are provided.

Oxygen is chosen to be the pure gas species, while the liquid consists of pure n-decane. Mass fraction freestream conditions correspond to those discussed in Section 4, with Y_1 representing the pure gas species composition. Thus, $Y_G = 1$ and $Y_L = 0$. Temperature (i.e., enthalpy) freestream conditions are $T(+\infty) = T_G = 550$ K and $T(-\infty) = T_L = 450$ K. Using the thermodynamic model, h_G and h_L are evaluated. Reynolds number, $Re_{\bar{L}}$, is based on gas properties and the relative velocity between the two free streams. To keep the boundary-layer approximation valid, freestream conditions for the streamwise velocity vary among the different analyzed pressures. Their values are summarized in Table 1.

In Section 6.1, the mixing layer solution from the system of ODEs is given for the four pressure cases from Table 1 and compared with the solution from the system of PDEs obtained in Davis et al. (2021) for the same configurations. Then, in Section 6.2, the interface equilibrium solution is compared between both approaches. Lastly, in Section 6.3, the evolution of the mass, momentum and thermal mixing layer thicknesses is determined and a generalization of their evaluation is made to avoid solving either the system of partial differential equations or the self-similar model.

6.1. Mixing layer profiles

For visualization purposes, the results are non-dimensionalized by the liquid freestream conditions to provide a consistent comparison between different cases. The non-dimensional similarity vari-

able and f function are, respectively,

$$\eta^* = \frac{\eta}{\sqrt{\frac{\rho_L \mu_L}{u_L}}} \quad ; \quad f^* = \frac{f}{\sqrt{\rho_L \mu_L u_L}} \tag{48}$$

The non-dimensional second derivative of f (or velocity gradient) follows that

$$f'' = \frac{d^2 f}{d\eta^2} = \frac{\sqrt{\rho_L \mu_L u_L}}{\frac{\rho_L \mu_L}{u_L}} \frac{d^2 f^*}{d\eta^{*2}} \quad ; \quad f''^* = \frac{f''}{\sqrt{\frac{u_L^3}{\rho_L \mu_L}}} \tag{49}$$

Any other variable, ϕ, is made dimensionless by dividing by the liquid freestream value, ϕ_L (e.g., $h^* = h/h_L$ or $f'^* = f'/u_L$). Note that Y is already non-dimensional. Furthermore, for continuous variables across the interface, such as f' and T, the following non-dimensional definitions are made to obtain distributions ranging from 0 to 1, being 1 the largest value of the variable,

$$\theta_T(\eta) = \frac{T(\eta) - T_L}{T_G - T_L} \quad ; \quad \theta_u(\eta) = \frac{f'(\eta) - u_G}{u_L - u_G} \tag{50}$$

The transformed transverse velocity, w, is not self-similar since it depends on $\bar{x}$ and η (see Eq. (19)). However, as stated in Section 3.1, w becomes a function of η only when multiplied by the square root of $\bar{x}$. Thus, $\hat{w} = w\sqrt{2\bar{x}} = \eta f' - f$ is self-similar. To obtain a non-dimensional $\hat{w}$ for representation purposes, the results are scaled as $\hat{w}^* = \hat{w}/\sqrt{\rho_L \mu_L u_L}$.

Fig. 2 presents the non-dimensional solution of f^*, f'^* and f''^*. Fig. 2b shows how the interface velocity tends to be very close to the freestream liquid velocity. That is, the liquid phase is much more dense and viscous than the gas phase and it becomes hard for the slower gas stream to slow the liquid stream down. The solutions of Y and h^* are plotted in Figs. 3 and 4.

As pressure increases well above the liquid critical pressure, the dissolution of the lighter gas species into the liquid phase is enhanced (Jordà-Juanós and Sirignano, 2015; Poblador-Ibanez and Sirignano, 2018) (see Fig. 3a). This generates sharper variations in the fluid properties within the liquid phase (see Fig. 5), which can be responsible for the change in behavior seen in the liquid velocity gradient. As seen in Fig. 2c, the velocity gradient behaves almost linearly within the liquid momentum mixing layer at subcritical pressures (i.e., 10 bar) where liquid density and viscosity remain fairly constant. However, as pressure increases well above the critical pressure of n-decane ($p_c = 21.03$ bar), the velocity gradient shows an inflection point where its rate of change experiences a transition from a stronger deceleration of the liquid near the interface to a slower deceleration in a larger portion of the mixing layer. These two differentiated regions match the region where density and viscosity are experiencing the largest drop towards interface values. That is, the less dense and viscous liquid phase is decelerated much more easily by the slower gas.

The specific mixture enthalpy distribution is consistent with the increase of temperature in the liquid phase and the decrease of temperature in the gas phase. However, a wavy distribution is observed at 10 bar. A discussion based on a thermodynamic analysis is provided in Poblador-Ibanez and Sirignano (2018). Considering a mass element containing the whole mixing layer (liquid and gas), the mixing process is just an internal phenomenon. Negligible net heat flux, Q, crosses the boundaries of the mass element. Therefore for a constant pressure process, $\Delta H = Q|_p = 0$. To compensate for the increase in enthalpy, H, in the liquid phase, the gas phase enthalpy must decrease accordingly. At 10 bar, this requirement cannot be solely satisfied with a monotonic enthalpy distribution.

Fig. 5 presents distributions for the non-dimensional density and viscosity for both phases. As previously mentioned, these fluid properties present sharper variations as pressure increases. As the mixture critical point is approached, both liquid and gas look more

Table 1
Freestream conditions for the streamwise component of the velocity field, u, at different ambient pressures. These values satisfy $Re_{\bar{L}} = 10,000$ at $\bar{L} = 0.01$ m for a fixed mean velocity of 10 m/s as the freestream gas density and viscosity change with pressure (Davis et al., 2021).

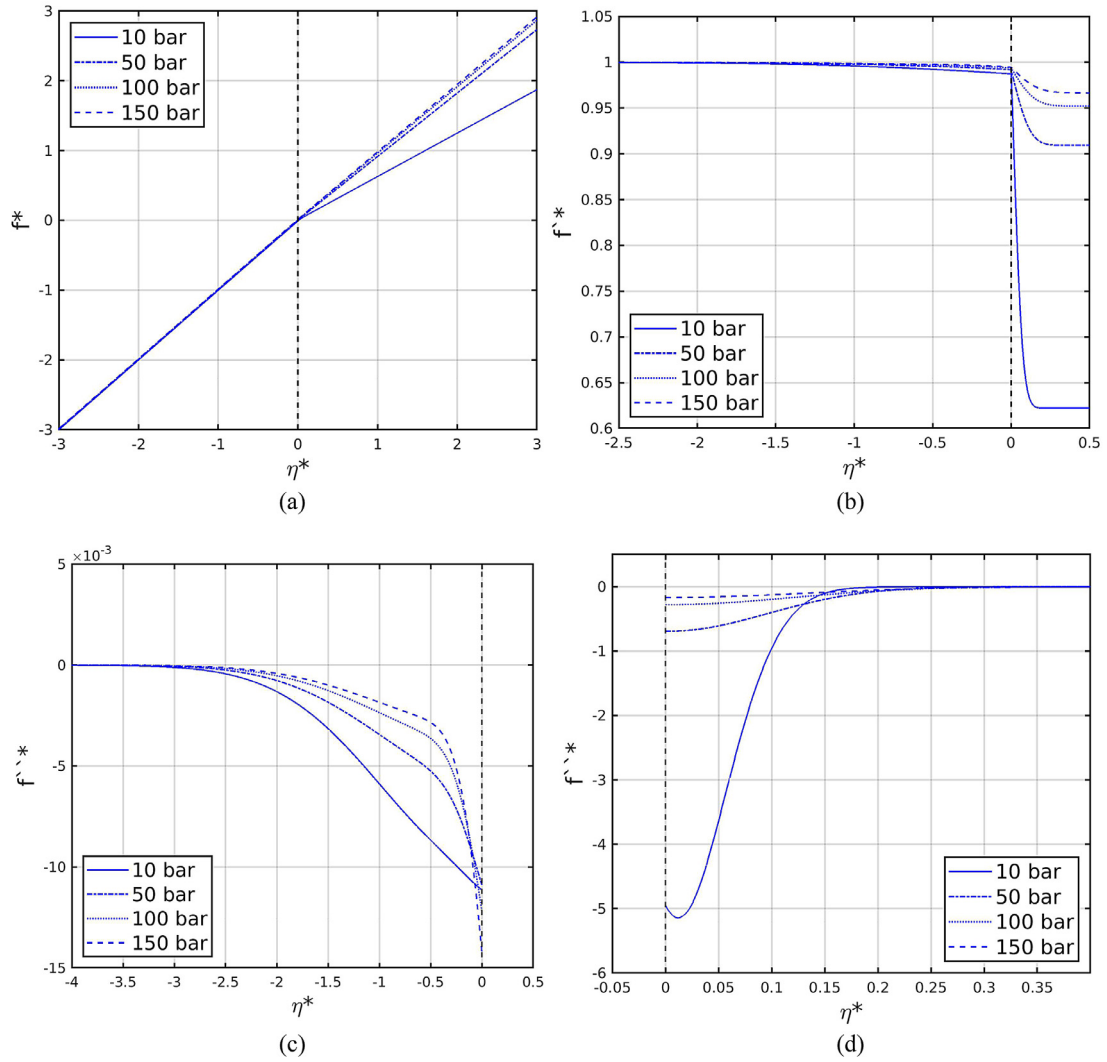|	$p = 10$ bar	$p = 50$ bar	$p = 100$ bar	$p = 150$ bar
u_G (m/s)	7.673	9.525	9.755	9.830
u_L (m/s)	12.327	10.475	10.246	10.170

Fig. 2. Solution of the self-similar system of ordinary differential equations. (a) $f*$; (b) $f'*$; (c) $f''*$ in the liquid phase; (d) $f''*$ in the gas phase.
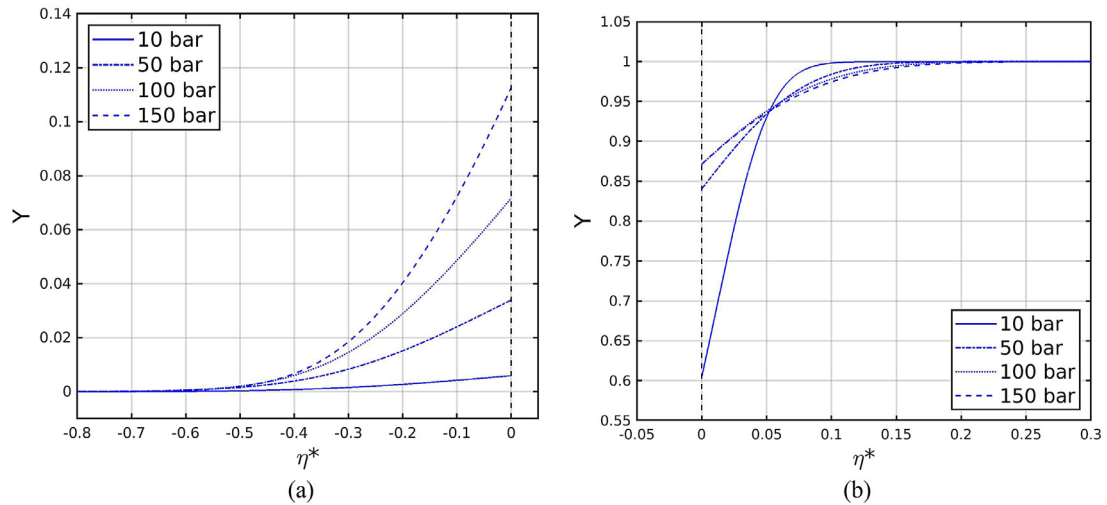

Fig. 3. Solution of the self-similar system of ordinary differential equations. (a) Y in the liquid phase; (b) Y in the gas phase.
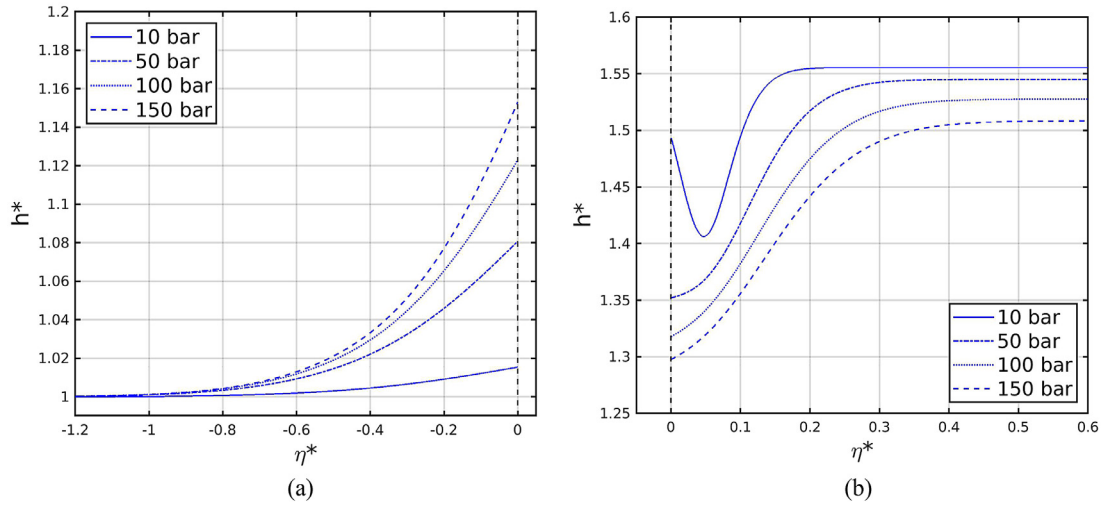
Fig. 4. Solution of the self-similar system of ordinary differential equations. (a) h^* in the liquid phase; (b) h^* in the gas phase.
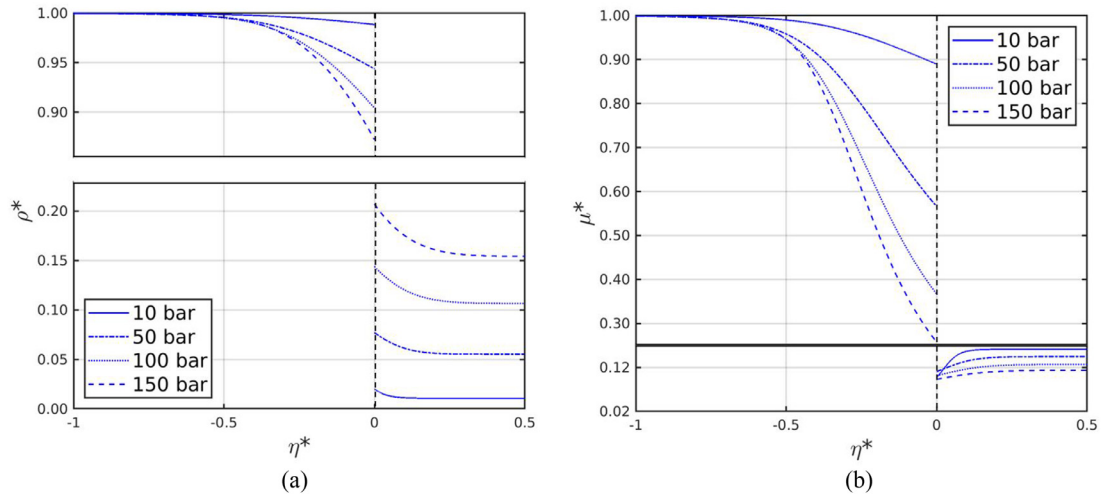

Fig. 5. Solution of the self-similar system of ordinary differential equations. (a) ρ^*; (b) μ^*.
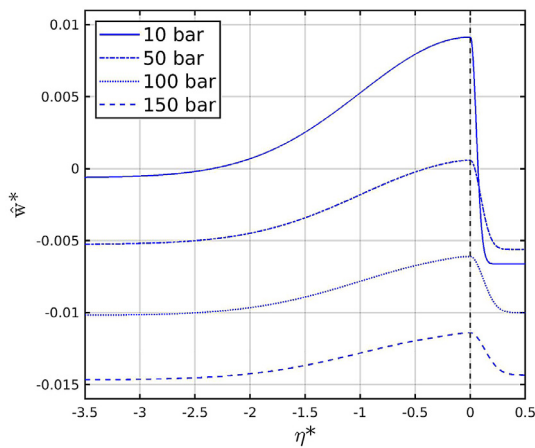

Fig. 6. $\hat{w}^*$ profiles from the solution of the self-similar system of ordinary differential equations.

alike. A discussion on the behavior of the viscosity profiles is provided in Davis et al. (2021).

Distributions of the non-dimensional modified transverse velocity, $\hat{w}^*$, are plotted in Fig. 6. Information on the phase change

behavior at the interface can be extracted from these results. At the interface, $w = \rho v$ from Eq. (9). Therefore, $w > 0$ or $\hat{w} > 0$ at the interface implies that the transverse velocity is also positive, $v > 0$. That is, net vaporization at the interface is occurring under the assumption that $V_\Gamma = 0$. On the other hand, $w < 0$ or $\hat{w} < 0$ implies $v < 0$ or net condensation. As inferred from Eq. (19), the strength of the mass flux across the interface decreases with downstream distance as $1/\sqrt{x}$ or $1/\sqrt{x}$. At 10 and 50 bar, net vaporization is occurring, while net condensation dominates at higher pressures. This interface behavior and its implications on the liquid jet breakup are further discussed in Poblador-Ibanez and Sirignano (2018, 2019).

The agreement between the solution of the self-similar system of ODEs and the system of PDEs is initially tested by comparing various profiles of different variables of interest. First, the PDE solution from Davis et al. (2021) at a downstream position of $x = 0.01$ m has been mapped from the (x, y) space to the η space for all four pressure cases.

Figs. 7 and 8 present these results for the non-dimensional distribution of continuous variables (i.e., θ_u and θ_T), where both methods are seen to concur for all analyzed pressures. As pressure increases and the gas dissolves more easily into the liquid phase, the interface velocity and temperature deviate further from the freestream liquid values. That is, as the liquid and gas phases
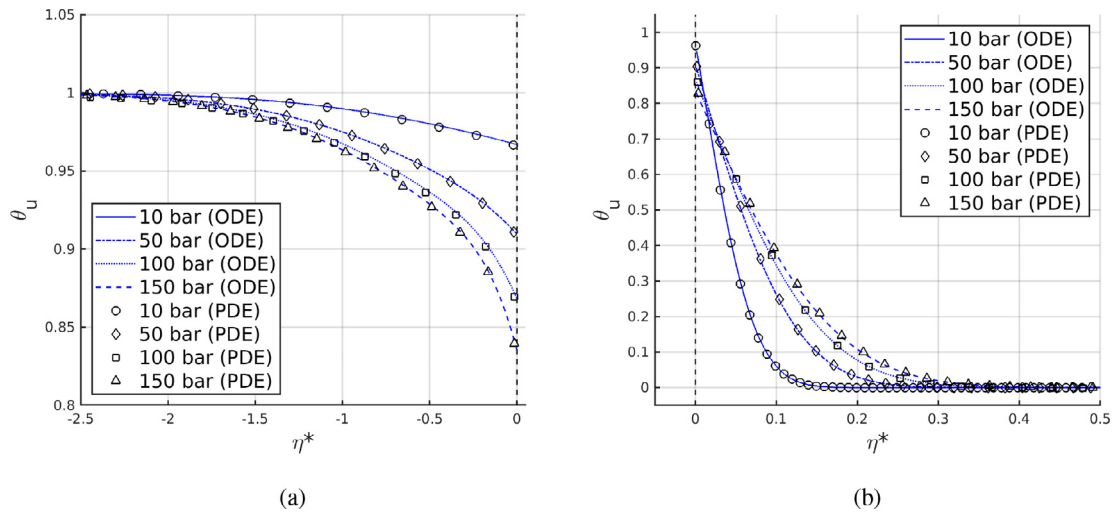
Fig. 7. Comparison between the solution of the system of ordinary differential equations (ODE) and the solution of the system of partial differential equations (PDE) at $x = 0.01$ m mapped from (x, y) to η. (a) θ_u in the liquid phase; (b) θ_u in the gas phase.
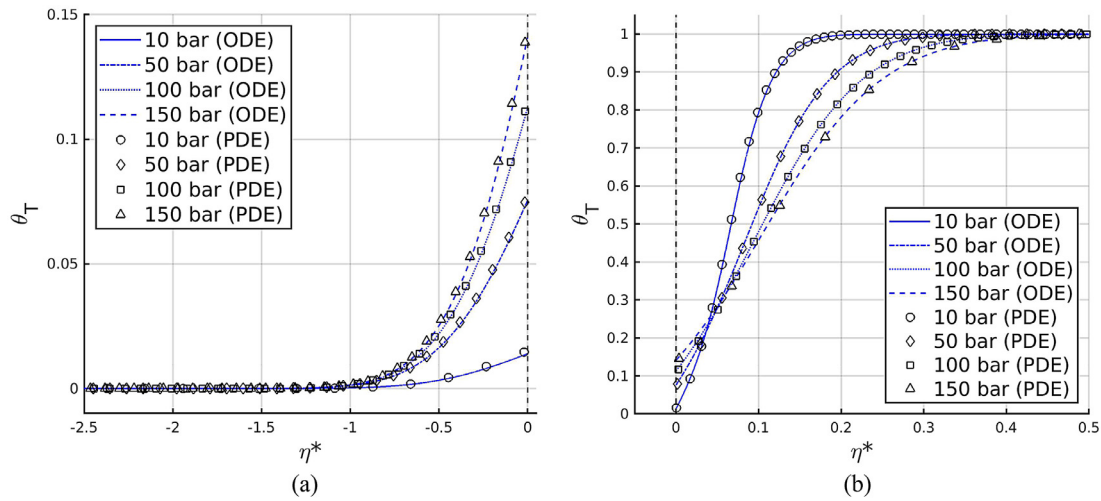

Fig. 8. Comparison between the solution of the system of ordinary differential equations (ODE) and the solution of the system of partial differential equations (PDE) at $x = 0.01$ m mapped from (x, y) to η. (a) θ_T in the liquid phase; (b) θ_T in the gas phase.

come closer together, the liquid loses inertia and the gas stream can slow it down more. Furthermore, the enhanced dissolution of the gas into the liquid increases the heat flux by diffusion into the liquid, raising its temperature near the interface.

Fig. 9 presents a comparison of $\hat{w}^*$ at 150 bar between the ODE solution and the PDE solution at $x = 0.01$ m. Two important issues can be observed in this figure. First, an offset exists between the ODE and the PDE profiles, which is related to slightly different interface equilibrium solutions, as shown in Section 6.2. Both the transverse velocity, v, and the modified transverse velocity, w, are variables with very small magnitudes compared to other flow parameters (e.g., temperature and density). Thus, relatively small differences of these variables at the interface can cause substantial relative errors in v and w. The evolution of v or w ultimately depend on a first-order ODE, with the interface value acting as the only needed boundary condition. When introducing a numerical offset as the difference between $w_{\Gamma, \text{ODE}}$ and $w_{\Gamma, \text{PDE}}$ (or being the same the difference between mass flux predictions at the interface, $\dot{\omega}_{\text{ODE}}$ and $\dot{\omega}_{\text{PDE}}$), the profiles are seen to collapse onto each other. Second, the PDE solution has some problems predicting the correct evolution of w in the liquid phase. From the ODE, w should be monotonically decreasing as $\eta^* \to -\infty$. However, the PDE so-

lution predicts a bump before decreasing. Refining the mesh used in Davis et al. (2021) mitigates the problem and the PDE solution tends asymptotically to the ODE solution. This issue has been identified as a numerical problem, but proper analysis of the error is out of scope of the present work.

Furthermore, the opposite mapping direction has been tested as well. That is, the ODE solution is mapped from the η space to the (x, y) space. Again, the main goal is to assess the validity of both approaches and identify numerical errors that might have arisen from the PDE-to-ODE domain mapping. Figs. 10–14 show the transverse profiles of different variables of interest (u, T, Y_1, ρ and v) at 150 bar at various downstream locations well into the self-similar region of the mixing layer. According to Davis et al. (2021), the mixing layer approximation with the boundary layer equations becomes valid for the analyzed configuration at 150 bar at $Re_x \approx 60$ in the gas mixing layer and $Re_x \approx 240$ in the liquid mixing layer, as defined by Eq. (5). This corresponds to a streamwise distance from the splitter plate of 0.06 mm and 0.24 mm, respectively. Following this restriction, the analyzed locations are $x = 1$ mm, $x = 5$ mm and $x = 10$ mm.

The profiles shown in Figs. 10–14 tend to collapse onto each other although some small deviations are seen depending on the

Table 2

Comparison of the interface velocity, U_Γ, equilibrium temperature, T_Γ, and equilibrium mixture specific enthalpies on each phase, h_g and h_l, between the solutions obtained using the system of ordinary differential equations (ODE) and the system of partial differential equations (PDE) (Davis et al., 2021).

p (bar)	$U_{\Gamma,ODE}$ (m/s)	$U_{\Gamma,PDE}$ (m/s)	$T_{\Gamma,ODE}$ (K)	$T_{\Gamma,PDE}$ (K)	$h_{g,ODE}$ (kJ/kg)	$h_{g,PDE}$ (kJ/kg)	$h_{l,ODE}$ (kJ/kg)	$h_{l,PDE}$ (kJ/kg)
10	12.173	12.171	451.397	451.497	488.874	489.153	332.414	332.696
50	10.389	10.389	457.547	457.610	444.511	444.624	355.320	355.498
100	10.182	10.181	461.276	461.326	437.012	437.093	372.448	372.589
150	10.114	10.114	464.095	464.121	434.971	435.013	386.550	386.624

Table 3

Comparison of the interface equilibrium composition on each phase, Y_{g,O_2} and Y_{l,O_2}, and equilibrium mixture densities on each phase, ρ_g and ρ_l, between the solutions obtained using the system of ordinary differential equations (ODE) and the system of partial differential equations (PDE) (Davis et al., 2021).

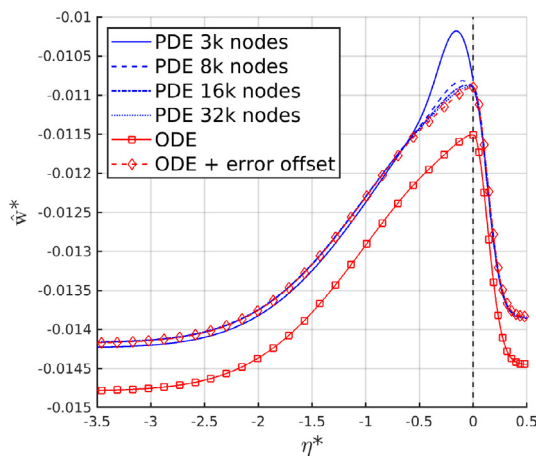| p (bar)	$Y_{g,O_2,ODE}$	$Y_{g,O_2,PDE}$	$Y_{l,O_2,ODE}$	$Y_{l,O_2,PDE}$	$\rho_{g,ODE}$ (kg/m³)	$\rho_{g,PDE}$ (kg/m³)	$\rho_{l,ODE}$ (kg/m³)	$\rho_{l,PDE}$ (kg/m³)
10	0.6059	0.6052	0.0059	0.0059	12.406	12.413	593.638	593.529
50	0.8405	0.8403	0.0339	0.0339	47.930	47.932	580.481	580.403
100	0.8712	0.8711	0.0716	0.0717	91.434	91.434	571.899	571.833
150	0.8714	0.8713	0.1126	0.1126	134.362	134.362	563.925	563.888

Fig. 9. Comparison of $\hat{w}^*$ at 150 bar between the solution of the system of ordinary differential equations (ODE) and the solution of the system of partial differential equations (PDE) at $x = 0.01$ m mapped from (x, y) to η.

variable and the fluid phase analyzed. The streamwise velocity and temperature profiles agree almost perfectly in both phases, but the mass fraction and density profiles deviate slightly.

Fig. 14 presents the transverse velocity profiles evaluated using Eq. (29). A mismatch between the ODE and the PDE solutions exist, which is easily observed in the profiles at $x = 1$ mm due to the larger magnitude of v at this location. Following what has been commented in previous paragraphs, small differences in the interface solution between the ODE and the PDE models are responsible for this mismatch. However, the profiles from both solutions evolve in a similar manner.

The results shown in Figs. 7–14 suggest that the non-ideal two-phase laminar mixing layer equations can be represented with a self-similar system of equations even though they are coupled to a complex thermodynamic model involving a cubic equation of state, high-pressure correlations used to evaluate transport properties, and non-ideal thermodynamic principles. To further compare the two approaches, Section 6.2 examines the interface solution obtained with the system of ODEs and the steady interface solution obtained far downstream of the splitter plate (i.e., $x = 0.01$ m) with the system of PDEs.

6.2. Interface equilibrium solution

This section compares the interface equilibrium solution obtained with the self-similar model with the results shown in

Davis et al. (2021) obtained with the mixing layer equations. To assess the performance of the self-similar system of equations, the error of a given variable Θ between the solution of the ODE system and the PDE system is defined as

$$E_\Theta = \frac{|\Theta_{ODE} - \Theta_{PDE}|}{|\Theta_{PDE}|} \qquad (51)$$

representing a relative deviation error from the PDE solution.

The interface values of different variables of interest (U_Γ, T_Γ, interface composition, etc.) obtained from the ODE and PDE solutions are shown in Tables 2–4. A very good agreement is seen for all variables except for the mass flux across the interface. Thus, relative errors are not provided when the error is a fraction of a percent.

The larger errors observed when comparing the mass flux across the interface at a given location (see Table 4) are of the order of 4–5% for 10, 100 and 150 bar while they are under 2% for the 50 bar case where the magnitude of the mass flux is the smallest. Nevertheless, the transition from net vaporization to net condensation is still well captured.

Sensitivity issues might arise when evaluating $\dot{\omega}$. Even though the relative errors in interface temperature, composition, etc. are near 0%, the magnitude of $\dot{\omega}$ itself is very small and easily perturbed by a small change in the other variables. This issue is then reflected in the transverse velocity profiles, as discussed in Section 6.1 and seen in Figs. 9 and 14, and might be one of the main causes of the small mismatch between the ODE and the PDE results when comparing mixing profiles across the mixing layer.

6.3. Mixing layer thickness

Discussion in prior subsections addressed the similarity of solutions at differing downstream positions for a given problem configuration. The similarity between cases with differing constraints is discussed in this section.

Table 4

Comparison of the net mass flux across the interface, $\dot{\omega}$, at the downstream location $x = \bar{x} = 0.01$ m between the solutions obtained using the system of ordinary differential equations (ODE) and the system of partial differential equations (PDE) (Davis et al., 2021).

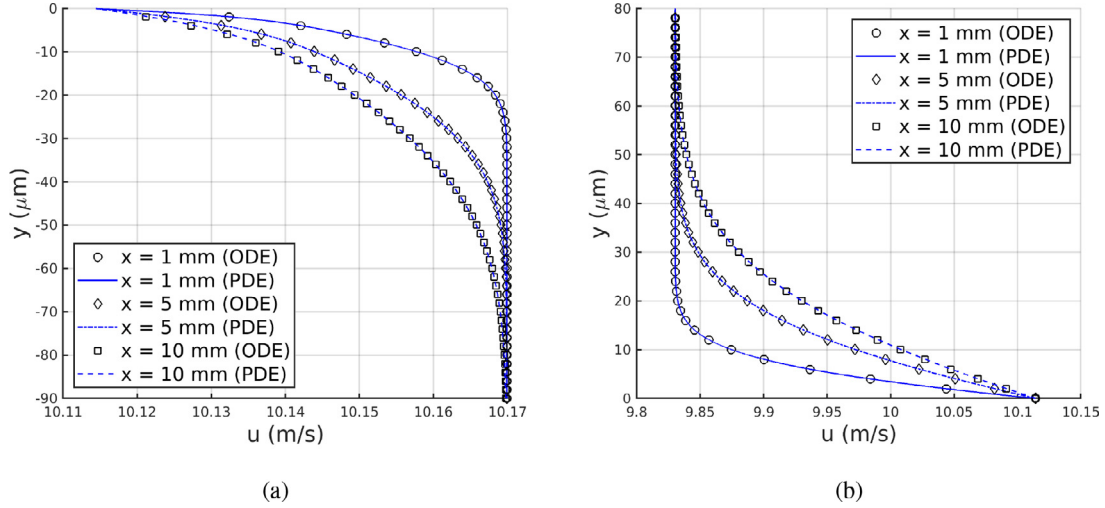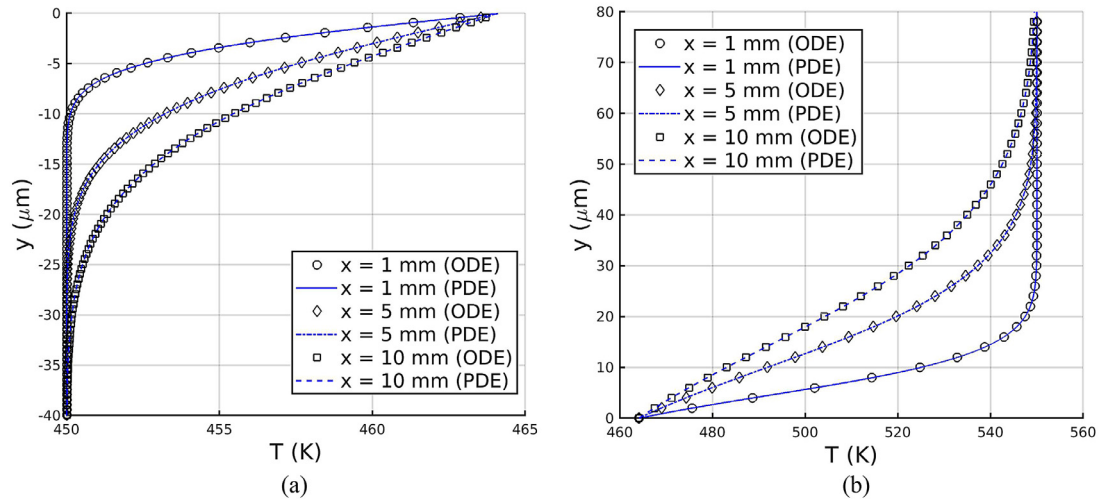| p (bar)	$\dot{\omega}_{ODE}$ (kg/m²s)	$\dot{\omega}_{PDE}$ (kg/m²s)	$E_{\dot{\omega}}$ (%)
10	0.0791	0.0760	4.079
50	0.00497	0.00488	1.844
100	-0.0565	-0.0539	4.824
150	-0.114	-0.109	4.587

Fig. 10. Comparison between the solution at 150 bar of the system of ordinary differential equations (ODE) and the solution of the system of partial differential equations (PDE) mapped from η to (x, y). (a) u in the liquid phase; (b) u in the gas phase.

Fig. 11. Comparison between the solution at 150 bar of the system of ordinary differential equations (ODE) and the solution of the system of partial differential equations (PDE) mapped from η to (x, y). (a) T in the liquid phase; (b) T in the gas phase.

The self-similar solution can provide information on the exact evolution of the mixing layer thickness. This is true for simpler analyses, such as the self-similar solution of incompressible flow over a flat plate (a.k.a., the Blasius equation) (White and Corfield, 2006). However, semi-empirical formulas are usually provided to estimate boundary layer or mixing layer thicknesses for more complex flows, such as compressible flows, with different boundary conditions (White and Corfield, 2006). These equations rely on many flow parameters and are not as accurate as obtaining the mixing layer thickness directly from the similarity solution of the specific constraints.

A more accurate approach is presented in this paper, which covers variable density flows under non-ideal conditions. It relies on solving the self-similar system of equations coupled with a non-ideal thermodynamic model. It is not as simple to implement as other semi-empirical models, but as discussed later, some generalization is possible. To evaluate the layer thickness on each side of the interface for mass, momentum and energy mixing regions, the following non-dimensional parameters are defined

$$\theta_{Y,l}^*(\eta) = \frac{Y_l(0) - Y(\eta)}{Y_l(0) - Y_L} \quad ; \quad \theta_{Y,g}^*(\eta) = \frac{Y(\eta) - Y_g(0)}{Y_G - Y_g(0)} \tag{52}$$

$$\theta_{u,l}^*(\eta) = \frac{U_\Gamma - u(\eta)}{U_\Gamma - U_L} \quad ; \quad \theta_{u,g}^*(\eta) = \frac{u(\eta) - U_\Gamma}{U_G - U_\Gamma} \tag{53}$$

$$\theta_{T,l}^*(\eta) = \frac{T_\Gamma - T(\eta)}{T_\Gamma - T_L} \quad ; \quad \theta_{T,g}^*(\eta) = \frac{T(\eta) - T_\Gamma}{T_G - T_\Gamma} \tag{54}$$

where all profiles vary from 0 to 1 going from the interface to the freestream condition. The mixture composition is used to analyze the mass mixing layer, while the streamwise velocity represents the momentum mixing layer. For the energy mixing layer, temperature has been used since it is a more representative variable than enthalpy. That is, the thermal mixing layer is represented, separately from composition influence on the enthalpy.

Davis et al. (2021) report the non-similarity across different problem constraints. However, when the proper fluid properties are used to non-dimensionalize the similarity variable and the mixing profiles, the thickness of the mixing layers almost collapse onto each other for different configurations. The analyzed cases are defined in Table 5. This is shown in Figs. 15–17. The profiles may also be nearly self-similar, although, in general, the variations in the behavior of the selected thermodynamic model creates different profiles as the problem configuration changes.
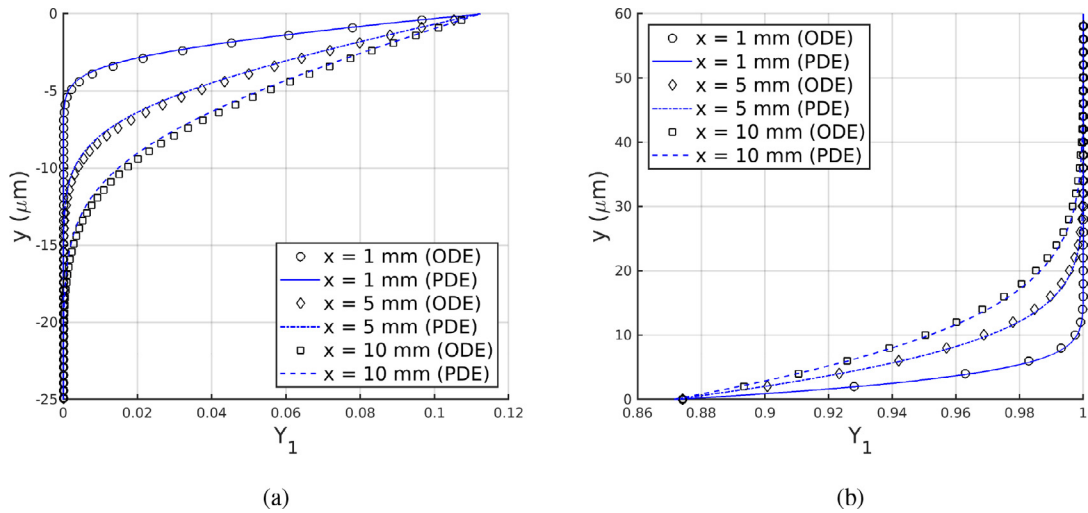
(a)

(b)

Fig. 12. Comparison between the solution at 150 bar of the system of ordinary differential equations (ODE) and the solution of the system of partial differential equations (PDE) mapped from η to (x, y). (a) Y_1 in the liquid phase; (b) Y_1 in the gas phase.
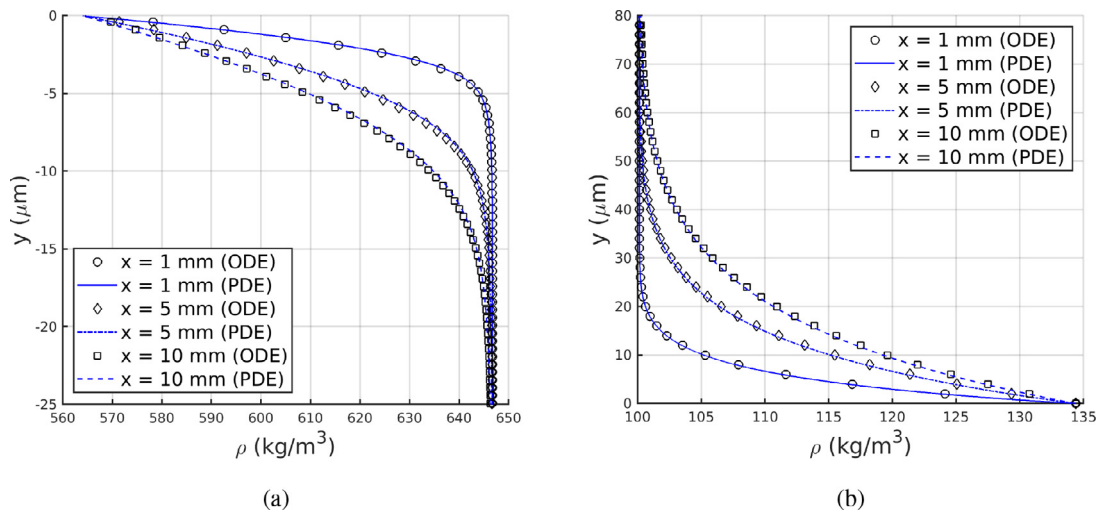

(a)

(b)

Fig. 13. Comparison between the solution at 150 bar of the system of ordinary differential equations (ODE) and the solution of the system of partial differential equations (PDE) mapped from η to (x, y). (a) ρ in the liquid phase; (b) ρ in the gas phase.
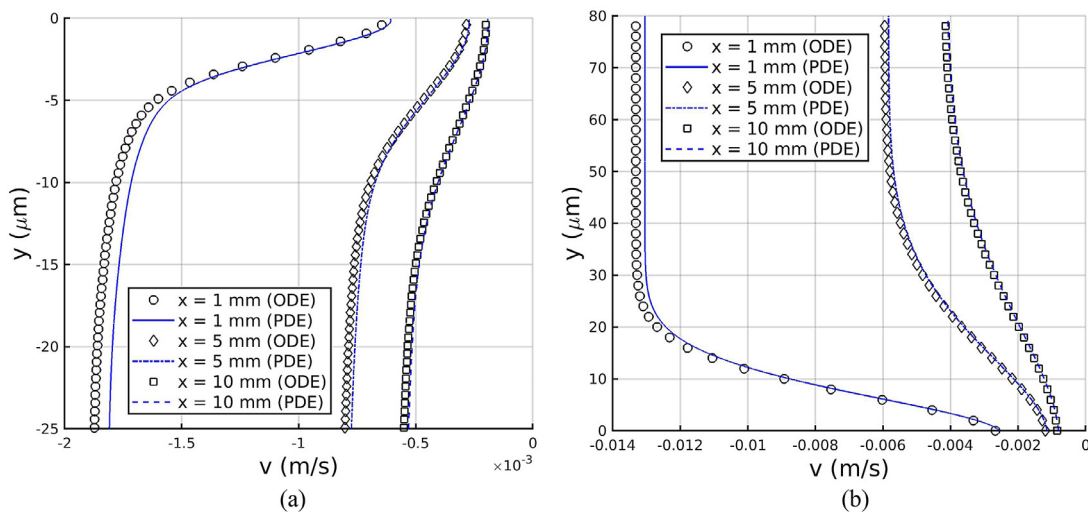

(a)

(b)

Fig. 14. Comparison between the solution at 150 bar of the system of ordinary differential equations (ODE) and the solution of the system of partial differential equations (PDE) mapped from η to (x, y). (a) v in the liquid phase; (b) v in the gas phase.

Fig. 15. Mass mixing layer thickness for different pressures, freestream velocities, freestream temperatures and mixture components. See Table 5 for reference. (a) liquid phase; (b) gas phase.

Fig. 16. Momentum mixing layer thickness for different pressures, freestream velocities, freestream temperatures and mixture components. See Table 5 for reference. (a) liquid phase; (b) gas phase.
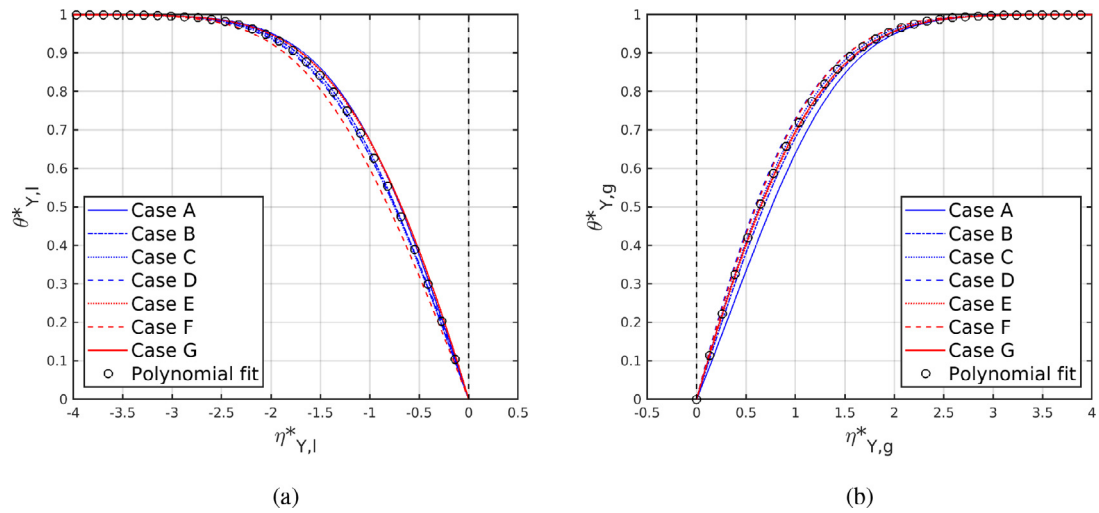

Fig. 17. Thermal mixing layer thickness for different pressures, freestream velocities, freestream temperatures and mixture components. See Table 5 for reference. (a) liquid phase; (b) gas phase.
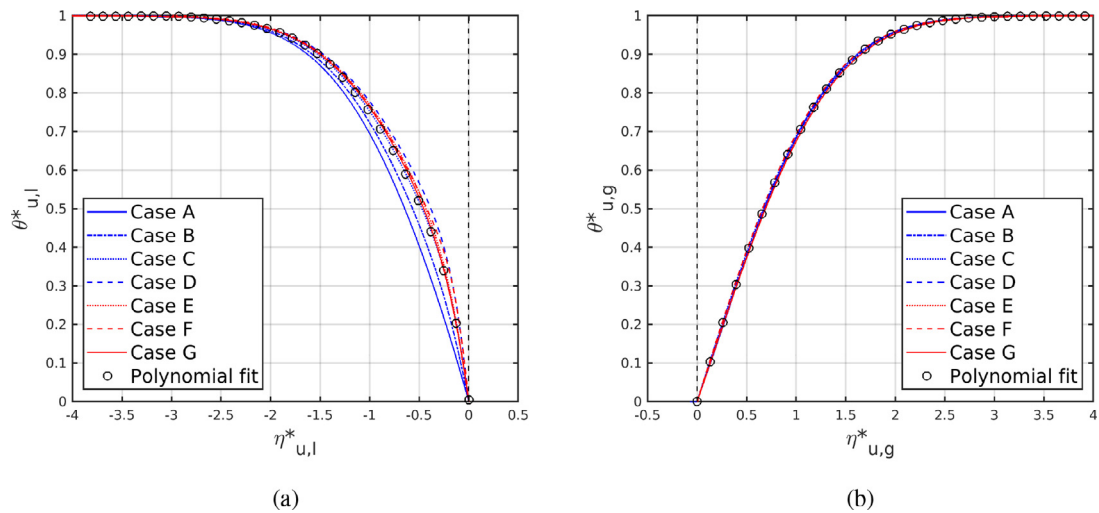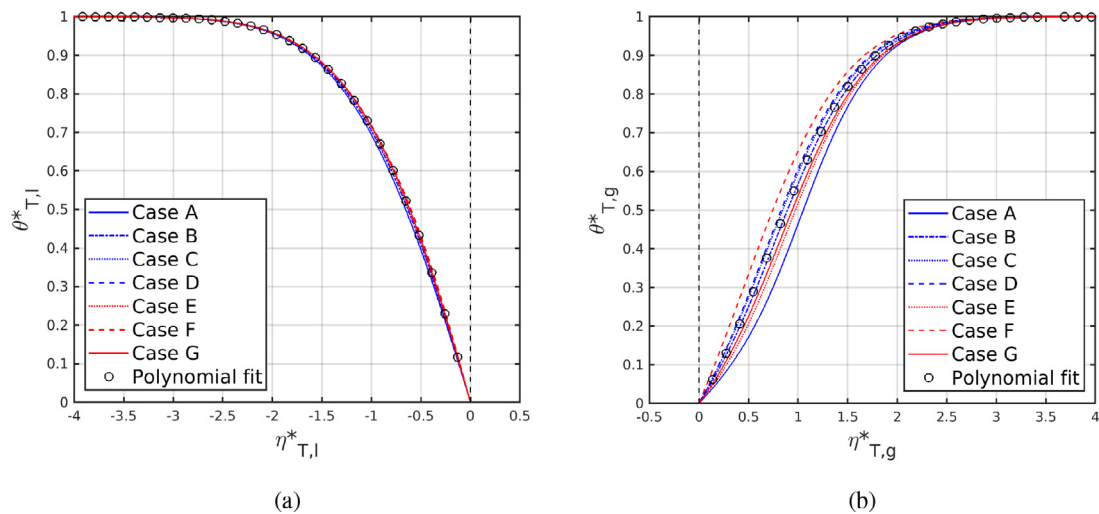
Table 5

Analyzed cases for the evaluation of the mixing layer thickness model. Cases A-D correspond to those analyzed in Davis et al. (2021).

Case	Mixture	p (bar)	u_G (m/s)	u_L (m/s)	T_G (K)	T_L (K)
A	$O_2/C_{10}H_{22}$	10	7.673	12.327	550	450
B	$O_2/C_{10}H_{22}$	50	9.525	10.475	550	450
C	$O_2/C_{10}H_{22}$	100	9.755	10.246	550	450
D	$O_2/C_{10}H_{22}$	150	9.830	10.170	550	450
E	$O_2/C_{10}H_{22}$	100	9.755	10.246	590	490
F	$O_2/C_{10}H_{22}$	150	9.830	10.170	510	410
G	O_2/C_8H_{18}	100	9.755	10.246	550	450

The non-dimensional similarity variables used to plot the mass mixing layer are defined from freestream conditions for each phase as

$$\eta_{Y,l}^* = \frac{\eta}{\sqrt{\frac{\rho_L^2 D_L}{u_L}}} \quad ; \quad \eta_{Y,g}^* = \frac{\eta}{\sqrt{\frac{\rho_G^2 D_G}{u_G}}} \tag{55}$$

and the non-dimensional similarity variables for the momentum mixing layer and the thermal mixing layer are defined, respectively, as

$$\eta_{u,l}^* = \frac{\eta}{\sqrt{\frac{\rho_L \mu_L}{u_L}}} \quad ; \quad \eta_{u,g}^* = \frac{\eta}{\sqrt{\frac{\rho_G \mu_G}{u_G}}} \tag{56}$$

and

$$\eta_{T,l}^* = \frac{\eta}{\sqrt{\frac{\rho_L \lambda_L}{c_{pL} u_L}}} \quad ; \quad \eta_{T,g}^* = \frac{\eta}{\sqrt{\frac{\rho_G \lambda_G}{c_{pG} u_G}}} \tag{57}$$

The mixing layer thickness, δ, is obtained by using Eq. (23). $\delta = \sqrt{2\bar{x}\bar{l}}(\eta)$ just represents the transverse coordinate evaluated at the η value defining the limit of the mixing layer. This limit is obtained from Eqs. (55)–(57), depending on the mixing layer being evaluated (i.e., mass, momentum or thermal). Note that the mixing layer thickness still evolves as a function of $\sqrt{x}$ whether the fluid experiences ideal or real conditions.

The diffusion layer thickness is defined at the location where θ^* is 99% of the difference between the freestream condition and the interface value. Using this definition, an exact value for the non-dimensional similarity variable, η^*, can be obtained for each case. Together with the $\rho(\eta)$ distribution obtained from the solution of the self-similar system of equations, the evaluation of δ is straightforward and it is an exact representation of the flow evolution under the self-similar analysis. However, this approach still depends on the solution of Eqs. (20)–(22) coupled with a thermodynamic model and does not yield an immediate estimate of the mixing layer thickness.

In view of the quasi-collapse of the location where the mixing layer ends and the reasonably similar diffusion profiles, the following approach is suggested. The main goal is to reduce the complexity of the exact evaluation of the mixing layer thickness

Table 7

Values of the non-dimensional similarity variables for mass, momentum and thermal mixing layer thicknesses obtained from the fitted polynomial. A range of values is also provided for the analyzed cases, together with a maximum relative deviation error from the polynomial value.

Mixing layer	η_{poly}^*	η_{min}^*	η_{max}^*	$\Delta_{\eta^*,max}$ (%)
$\eta_{Y,l}^*$	−2.672	−2.785	−2.589	4.229
$\eta_{Y,g}^*$	2.515	2.459	2.576	2.425
$\eta_{u,l}^*$	−2.498	−2.561	−2.410	3.523
$\eta_{u,g}^*$	2.548	2.510	2.579	1.491
$\eta_{T,l}^*$	−2.541	−2.559	−2.533	0.708
$\eta_{T,g}^*$	2.683	2.564	2.724	4.435

to a simpler model relying on freestream conditions and interface properties, coupled only with an equation of state. Therefore, it is no longer needed to solve the system of ODEs and the diffusion process within the mixing layer, as long as the interface solution is already known (e.g., it could be possible to tabulate interface solutions based on the thermodynamic model and problem configuration).

A polynomial of degree 9 is fitted using a least-squares method among the data defining the distributions of mass fraction, velocity and temperature within the mixing layer for each case. That is, the following function is used to represent the diffusion profiles

$$p(\eta^*) = \sum_{i=1}^{n=10} p_i \eta^{*^{n-i}} \tag{58}$$

where $p(\eta^*)$ represents $\theta_{Y,l}^*(\eta_{Y,l}^*)$, $\theta_{Y,g}^*(\eta_{Y,g}^*)$, $\theta_{u,l}^*(\eta_{u,l}^*)$, $\theta_{u,g}^*(\eta_{u,g}^*)$, $\theta_{T,l}^*(\eta_{T,l}^*)$ or $\theta_{T,g}^*(\eta_{T,g}^*)$. The polynomial reasonably predicts the diffusion profiles with the exception of the gas temperature profile and the liquid streamwise velocity profile, where larger variations are observed (see Figs. 15–17). The coefficients of Eq. (58) to predict each distribution are given in Table 6.

A representative value of η^* defining the mixing layer thickness for all scenarios is obtained from the polynomial fitting of each profile (i.e., where each polynomial profile reaches 99% of the freestream value). Table 7 provides information about these values for each non-dimensional similarity variable, as well as a range of observed values in all cases. Varying pressure, temperature freestream values, freestream velocities and mixture components resulted in very similar η^* values, with maximum relative deviations, Δ, from the polynomial solution below 5%.

Based solely on the freestream conditions and the interface properties, a distribution in terms of the similarity variable, η, can be obtained for temperature and mass fraction. Using an equation of state, such as the volume-corrected SRK equation of state, a distribution for density or $\rho(\eta)$ is found. The values for η^* obtained with the fitted polynomials define the integration limit of Eq. (23); therefore, the equation can be solved and an estimate for the mixing layer thickness is obtained.

Table 6

Coefficients of the polynomial fit of $\theta_{Y,l}^*(\eta_{Y,l}^*)$, $\theta_{Y,g}^*(\eta_{Y,g}^*)$, $\theta_{u,l}^*(\eta_{u,l}^*)$, $\theta_{u,g}^*(\eta_{u,g}^*)$, $\theta_{T,l}^*(\eta_{T,l}^*)$ and $\theta_{T,g}^*(\eta_{T,g}^*)$.

Polynomial	$\theta_{Y,l}^*(\eta_{Y,l}^*)$	$\theta_{Y,g}^*(\eta_{Y,g}^*)$	$\theta_{u,l}^*(\eta_{u,l}^*)$	$\theta_{u,g}^*(\eta_{u,g}^*)$	$\theta_{T,l}^*(\eta_{T,l}^*)$	$\theta_{T,g}^*(\eta_{T,g}^*)$
$p_1 \times 10^4$	0.15167	0.19023	−3.29382	0.21758	0.10990	1.02187
$p_2 \times 10^4$	−4.23064	−4.66887	−78.0620	−5.33430	2.69978	−26.3374
$p_3 \times 10^3$	−4.90381	4.69201	−78.5302	5.33306	2.92476	28.3791
$p_4 \times 10^2$	−3.01070	−2.41875	−43.6676	−2.70735	1.87074	−16.4236
$p_5 \times 10^2$	−10.1995	6.30927	−146.378	6.69482	7.86786	54.0947
$p_6 \times 10^1$	−1.74246	−0.56551	−30.2891	−0.37532	2.17118	−9.66246
$p_7 \times 10^1$	−1.10601	−0.41711	−38.4520	−1.37345	3.23844	7.32169
$p_8 \times 10^1$	−1.44243	−1.40570	−30.5828	0.29545	−0.27706	−0.41950
$p_9 \times 10^1$	−7.79459	8.99477	−18.8875	7.85479	−9.08996	4.50979
$p_{10} \times 10^4$	−5.29066	−0.24932	49.3394	0.27385	−3.26408	−4.58044

Table 8

Maximum relative deviations from the exact ODE solution within the diffusion layer using the fitted polynomial together with freestream conditions and interface properties to solve for $Y(\eta)$, $u(\eta)$, $T(\eta)$ and, coupled with the volume-corrected SRK equation of state, $\rho(\eta)$. For the mass fraction, the maximum absolute deviation is considered.

| Case	$\Delta_{Y_l,\max}$ (%)	$\Delta_{Y_g,\max}$ (%)	$\Delta_{u_l,\max}$ (%)	$\Delta_{u_g,\max}$ (%)	$\Delta_{T_l,\max}$ (%)	$\Delta_{T_g,\max}$ (%)	$\Delta_{\rho_l,\max}$ (%)	$\Delta_{\rho_g,\max}$ (%)
A	0.0153	3.1645	0.1563	0.3438	0.0229	2.3583	0.0044	4.3184
B	0.0345	0.4553	0.0529	0.0228	0.0145	0.2429	0.0546	0.5676
C	0.1082	0.0438	0.0031	0.0157	0.0089	0.3398	0.1200	0.3725
D	0.1652	0.3640	0.0362	0.0190	0.0292	0.4943	0.1355	0.6826
E	0.1879	0.3263	0.0198	0.0397	0.0083	1.1313	0.2992	1.3712
F	0.5118	0.1326	0.0267	0.0250	0.0400	1.5627	0.3429	1.7818
G	0.2575	0.1795	0.0107	0.0430	0.0090	0.7723	0.3439	0.9377
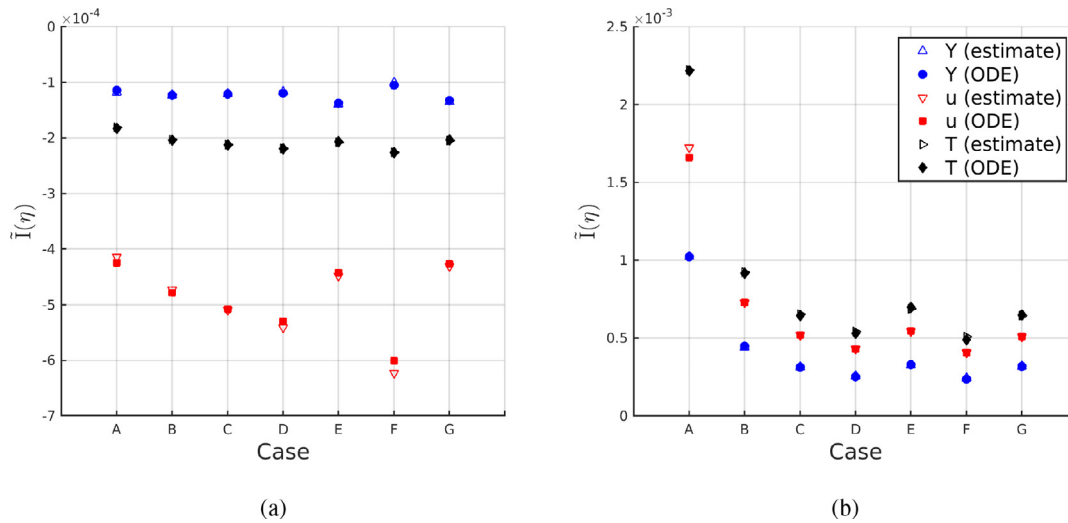
Fig. 18. Comparison of the evaluation of mixing layer thickness between the exact solution of the ODE system and the approximate method based on the fitted polynomial. (a) liquid phase; (b) gas phase.

Table 8 shows the maximum deviation errors between the exact solution obtained from the system of ODEs and the approximate diffusion profiles obtained from the polynomial fit. Relative errors are provided for streamwise velocity, temperature and density solutions, while absolute errors are provided for the mass fraction profiles. Errors are seen to be limited well below 5% for the analyzed cases, being negligible in some scenarios. Note the small error in estimating the velocity profile. The profiles in the gas phase collapse almost perfectly, thus generating small deviations between exact solutions and estimated values. This situation also happens for the liquid temperature profile. However, the velocity profiles in the liquid phase showed greater variations between each other. Nevertheless, the interface streamwise velocity tends to be very close to the liquid freestream velocity for all analyzed cases. Therefore, the magnitude errors between the exact solution and the polynomial estimate are very small even though $\theta^*_{u,l}$ profiles do not collapse onto each other.

The difference in the evaluation of the integral from Eq. (23) or $\tilde{I}(\eta)$, i.e., whether the exact solution of the ODE system or the approximate method is used, causes different mixing layer thicknesses. Fig. 18 shows the value of this integral where 99% of the freestream value is obtained using both approaches. Overall, estimated values are in good agreement with the ODE solution. The relative deviation error of the mixing layer thickness value from the exact ODE solution is shown in Fig. 19. In general, errors are small and below 2%. However, some estimates present higher errors, but still below 5%.

Information on the mixing layer thickness can be directly obtained from Fig. 18. As previously mentioned, the magnitude of $\tilde{I}(\eta)$ is used to estimate the mixing layer thickness at any downstream location as $\delta = \sqrt{2\bar{x}}\tilde{I}(\eta)$. It is interesting to note that while
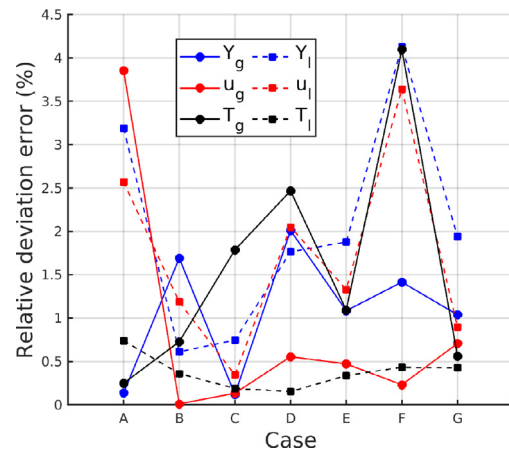

Fig. 19. Relative deviation error from the exact ODE solution of mixing layer thickness for the different mixing layers on each phase.

the thermal mixing layer is always larger in the gas phase, the momentum mixing layer dominates by a larger factor in the liquid phase. In both phases, the mass mixing layer is the smallest.

The effects of increasing pressure on the mixing layer thickness are shown through cases A-D. The gas becomes more dense as pressure increases, reducing diffusivity. Thus, the gas mixing layer becomes thinner at larger pressures. On the other hand, the increased solubility of the gas into the liquid when pressure increases widens the momentum and thermal mixing layers in the liquid phase.
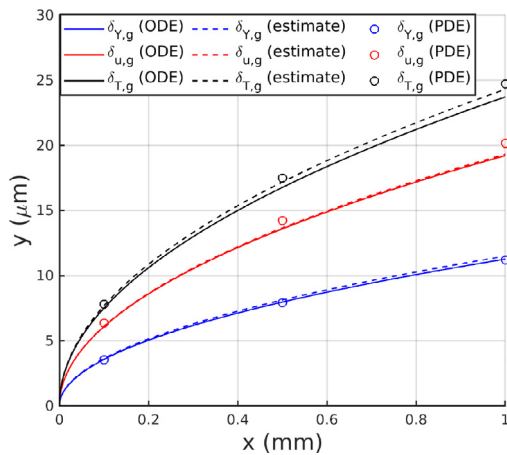
Fig. 20. Mass, momentum and thermal gas mixing layer thickness evolution for case D (see Table 5). A comparison between the ODE solution, the polynomial approximation and the PDE solution is presented.

Fig. 20 presents the evolution of the mass, momentum and thermal gas mixing layers for case D (i.e., a very high pressure case). The mixing layer thickness is computed using Eq. (23) and a comparison between the solution obtained with the exact ODE solution and the polynomial estimation is shown. Furthermore, data points from the PDE solution obtained in Davis et al. (2021) are overlapped. The mixing layer thicknesses based on the PDE solution are obtained as the transverse location, y, where $\theta_{Y,g}$, $\theta_{u,g}$ and $\theta_{T,g}$ become 0.99.

The evolution of the different mixing layer thicknesses is in accordance for the three methods used in this comparison. Errors between the ODE solution and the estimated solution based on the polynomial fit have already been discussed (see Fig. 19). For both of them, the mixing layer must grow with downstream distance as $\sqrt{x}$, which is corroborated with the PDE results from Davis et al. (2021). However, deviations between the self-similar model and the mixing layer equations are seen, especially for the evolution of the streamwise velocity and the temperature mixing layers, with errors of the same order as the relative deviations between the ODE solution and the approximate solution ($< 5\%$).

Overall, the polynomial fitting approach is valid for the type of mixture and range of thermodynamic states evaluated in this work. It simplifies the evaluation of the mixing layer thickness with reasonable accuracy and only relies on the freestream conditions and the interface solution, which could be tabulated from previous simulations. Thus, it is not necessary to solve the system of ODEs or the system of PDEs for all cases and an estimate of the mixing layer thicknesses can be readily obtained. It is expected that other problem configurations not used in the development of the correlations could show larger errors than the ones reported for cases A–G.

7. Summary and conclusions

The non-ideal, two-phase, laminar mixing-layer equations have been reduced to a system of ordinary differential equations in terms of a similarity variable, η. The similarity transformation follows classical techniques used in compressible flows (Williams, 2018) and has been generalized to be implemented with any non-ideal thermodynamic model for the equation of state and local phase equilibrium at the liquid-gas interface. In this work, the high-pressure thermodynamic model is based on a volume-corrected Soave-Redlich-Kwong cubic equation of state and other fundamental thermodynamic principles, coupled with high-

pressure correlations to evaluate transport coefficients and phase equilibrium (Davis et al., 2021).

Good agreement between the self-similar solution and the solution of the system of partial differential equations (Davis et al., 2021) is obtained, proving the validity of the self-similar approach. This is an important step towards reducing the complexity of the analysis of supercritical two-phase flows, while still capturing the main physics involved (e.g., enhanced diffusivity in the liquid phase, phase change reversal at the interface). This type of approach can be helpful when used to implement realistic initial conditions to more complex flow simulations (i.e., high-pressure atomization). The results show the existence of two phases at pressures above the critical pressure of any chemical component. It is seen that net condensation can occur even though the gas is hotter and heat is conducting into the liquid, as reported in previous works (Poblador-Ibanez and Sirignano, 2018; 2019).

A correlation using a ninth-order polynomial is used to fit data from various problem configurations into a generalized approach to represent the mixing layer evolution. This reduces the set of ordinary differential equations to a set of functions which depend only on the freestream conditions, the interface equilibrium solution and a non-ideal equation of state. Good estimates of the evolution of the mixing layer thickness on both sides of the interface are obtained from this simplified model, with errors well below 5% in most cases.

Declaration of Competing Interest

The authors declared that there is no conflict of interest.

CRediT authorship contribution statement

Jordi Poblador-Ibanez: Conceptualization, Methodology, Software, Validation, Formal analysis, Data curation, Writing - original draft, Writing - review & editing, Visualization. **Branson W. Davis:** Conceptualization, Software, Data curation, Writing - review & editing. **William A. Sirignano:** Conceptualization, Writing - review & editing, Supervision, Funding acquisition.

Acknowledgments

References

Chehroudi, B., 2012. Recent experimental efforts on high-pressure supercritical injection for liquid rockets and their implications. Int. J. Aerosp. Eng. 2012, 1–30.

Chehroudi, B., Cohn, R., Talley, D., 2002. Cryogenic shear layers: experiments and phenomenological modeling of the initial growth rate under subcritical and supercritical conditions. Int. J. Heat Fluid Flow 23 (5), 554–563.

Chehroudi, B., Talley, D., Coy, E., 2002. Visual characteristics and initial growth rates of round cryogenic jets at subcritical and supercritical pressures. Phys. Fluids 14 (2), 850–861.

Chung, T.H., Ajlan, M., Lee, L.L., Starling, K.E., 1988. Generalized multiparameter correlation for nonpolar and polar fluid transport properties. Ind. Eng. Chem. Res. 27 (4), 671–679.

Dahms, R.N., Oefelein, J.C., 2013. On the transition between two-phase and single-phase interface dynamics in multicomponent fluids at supercritical pressures. Phys. Fluids 25 (9), 092103.

Dahms, R.N., Oefelein, J.C., 2015. Liquid jet breakup regimes at supercritical pressures. Combust. Flame 162 (10), 3648–3657.

Dahms, R.N., Oefelein, J.C., 2015. Non-equilibrium gas-liquid interface dynamics in high-pressure liquid injection systems. Proc. Combust. Inst. 35 (2), 1587–1594.

Davis, B.W., Poblador-Ibanez, J., Sirignano, W.A., 2021. Two-phase developing laminar mixing layer at supercritical pressures. Int. J. Heat. Mass Transf. 167, 120687.

Delplanque, J.-P., Sirignano, W.A., 1993. Numerical study of the transient vaporization of an oxygen droplet at sub- and supercritical conditions. Int. J. Heat Mass Transf. 36 (2), 303–314.

Dorodnitsyn, A., 1942. Boundary layer in a compressible gas. Prikl. Mat. Mekh. 6 (6), 449–486.

Falgout, Z., Rahm, M., Sedarsky, D., Linne, M., 2016. Gas/fuel jet interfaces under high pressures and temperatures. Fuel 168, 14–21.

Mayer, W.O.H., Schik, A.H.A., Vielle, B., Chauveau, C., Gökalp, I., Talley, D.G., Woodward, R.D., 1998. Atomization and breakup of cryogenic propellants under high-pressure subcritical and supercritical conditions. J. Propul. Power 14 (5), 835–842.

He, P., Ghoniem, A.F., 2017. A sharp interface method for coupling multiphase flow, heat transfer and multicomponent mass transfer with interphase diffusion. J. Comput. Phys. 332, 316–332.

Howarth, L., 1948. Concerning the effect of compressibility on laminar boundary layers and their separation. Proc. R. Soc. London Ser.A 194 (1036), 16–42.

Hsieh, K.C., Shuen, J.S., Yang, V., 1991. Droplet vaporization in high-pressure environments i: near critical conditions. Combust. Sci. Technol. 76 (1–3), 111–132.

Jarrahbashi, D., Sirignano, W.A., 2014. Vorticity dynamics for transient high-pressure liquid injection. Phys. Fluids 26 (10), 101304.

Jarrahbashi, D., Sirignano, W.A., Popov, P.P., Hussain, F., 2016. Early spray development: hole, ligament and bridge formations. J. Fluid Mech. 792, 186–231.

Jordà-Juanós, A., Sirignano, W.A., 2015. Thermodynamic analysis for combustion at high gas densities. In: Proceedings of the 25th ICDERS. Leeds, UK: ICDERS.

Kennedy, C.A., Gatski, T.B., 1994. Self-similar supersonic variable-density shear layers in binary systems. Phys. Fluids 6 (2), 662–673.

Leahy-Dios, A., Firoozabadi, A., 2007. Unified model for nonideal multicomponent molecular diffusion coefficients. AIChE J. 53 (11), 2932–2939.

Lees, L., 1956. Laminar heat transfer over blunt-nosed bodies at hypersonic flight speeds. J. Jet Propul. 26 (4), 259–269.

Libby, P.A., Liu, T., 1968. Some similar laminar flows obtained by quasilinearization.. AIAA J. 6 (8), 1541–1548.

Lin, H., Duan, Y.-Y., Zhang, T., Huang, Z.-M., 2006. Volumetric property improvement for the Soave- Redlich- Kwong equation of state. Ind. Eng. Chem. Res. 45 (5), 1829–1839.

Mayer, W.O.H., Schik, A.H.A., Schaffler, M., Tamura, H., 2000. Injection and mixing processes in high-pressure liquid oxygen/gaseous hydrogen rocket combustors. J. Propul. Power 16 (5), 823–828.

Mayer, W.O.H., Tamura, H., 1996. Propellant injection in a liquid oxygen/gaseous hydrogen rocket engine. J. Propul. Power 12 (6), 1137–1147.

Minniti, M., Ziaee, A., Curran, D., Porter, J., Parker, T., Dunn-Rankin, D., 2019. Femtosecond digital holography in the near-nozzle region of a dodecane spray. At. Sprays 29 (3), 251–267.

Minniti, M., Ziaee, A., Trolinger, J., Dunn-Rankin, D., 2018. Ultrashort pulse off-axis digital holography for imaging the core structure of transient sprays. At. Sprays 28 (6), 565–578.

Oschwald, M., Smith, J.J., Branam, R., Hussong, J., Schik, A.H.A., Chehroudi, B., Talley, D., 2006. Injection of fluids into supercritical environments. Combust. Sci. Technol. 178 (1–3), 49–100.

Poblador-Ibanez, J., Sirignano, W.A., 2018. Transient behavior near liquid-gas interface at supercritical pressure. Int. J. Heat Mass Transf. 126, 457–473.

Poblador-Ibanez, J., Sirignano, W.A., 2019. Analysis of an axisymmetric liquid jet at supercritical pressures. In: Proceedings of the ILASS-Americas 30th Annual Conference on Liquid Atomization and Spray Systems, Tempe, AZ.

Poling, B.E., Prausnitz, J.M., John Paul, O., Reid, R.C., 2001. The Properties of Gases and Liquids, vol. 5. McGraw-Hill New York.

Prausnitz, J.M., Tavares, F.W., 2004. Thermodynamics of fluid-phase equilibria for standard chemical engineering operations. AIChE J. 50 (4), 739–761.

Pruett, C.D., 1993. On the accurate prediction of the wall-normal velocity in compressible boundary-layer flow. Int. J. Numer. Methods Fluids 16 (2), 133–152.

Rosner, D., 1967. On liquid droplet combustion at high pressures. AIAA J. 5 (1), 163–166.

Segal, C., Polikhov, S.A., 2008. Subcritical to supercritical mixing. Phys. Fluids 20 (5), 052101.

Sirignano, W.A., 2021. Mixing and combustion in a laminar shear layer with imposed counterflow. J. Fluid Mech. 908, A35.

Sirignano, W.A., Delplanque, J.-P., Liu, F., 1997. Selected challenges in jet and rocket engine combustion research. In: 33rd Joint Propulsion Conference and Exhibit, p. 2701.

Soave, G., 1972. Equilibrium constants from a modified Redlich-Kwong equation of state. Chem. Eng. Sci. 27 (6), 1197–1203.

Spalding, D., 1959. Theory of particle combustion at high pressures. ARS J. 29 (11), 828–835.

Stewartson, K., 1949. Correlated incompressible and compressible boundary layers. Proc. R. Soc. London Ser.A 200 (1060), 84–100.

White, F.M., Corfield, I., 2006. Viscous Fluid Flow, vol. 3. McGraw-Hill New York.

Williams, F.A., 2018. Combustion Theory. CRC Press.

Yang, V., 2000. Modeling of supercritical vaporization, mixing, and combustion processes in liquid-fueled propulsion systems. Proc. Combust. Inst. 28 (1), 925–942.

Yang, V., Shuen, J.-S., 1994. Vaporization of liquid oxygen (LOX) droplets in supercritical hydrogen environments. Combust. Sci. Technol. 97 (4–6), 247–270.

Zandian, A., Sirignano, W.A., Hussain, F., 2017. Planar liquid jet: Early deformation and atomization cascades. Phys. Fluids 29 (6), 062109.

Zandian, A., Sirignano, W.A., Hussain, F., 2018. Understanding liquid-jet atomization cascades via vortex dynamics. J. Fluid Mech. 843, 293–354.

Zandian, A., Sirignano, W.A., Hussain, F., 2019. Length-scale cascade and spread rate of atomizing planar liquid jets. Int. J. Multiph. Flow 113, 117–141.